Tuning Physical Properties of NiFe$_2$O$_4$ and NiFe$_2$O$_4$@SiO$_2$ Nanoferrites by Thermal Treatment

A. BAJOREK, C. BERGER, M. DULSKI, M. ZUBKO, S. LEWIŃSKA, K. PRUSIK, A. ŚLAWSKA-WANIEWSKA, F. GRASSET, and N. RANDRIANANTOANDRO

The comparison between NiFe$_2$O$_4$ (co-precipitation) and NiFe$_2$O$_4$@SiO$_2$ (co-precipitation and microemulsion) ferrite nanoparticles in their as-received and annealed form is presented. The structural characterization revealed the gradual crystallization of as-received samples induced by thermal treatment. The existence of cubic inverse spinel ferrite structure with tetrahedral and octahedral iron occupancy is confirmed in all samples by the comprehensive study. The Fourier-transform infrared (FTIR) spectroscopy confirmed the typical spinel structure and other Fe-based states, whereas the presence of nonstoichiometric hematite is detected in the annealed NiFe$_2$O$_4$ sample. In the case of nanoparticles embedded into the silica matrix, the crystallization of initially amorphous silica is revealed in structural and microstructural characterization. As shown by FTIR, the applied thermal treatment reduces the water molecules and hydroxyl units compared to the initial material. The separation of the rhombohedral hematite α-Fe$_2$O$_3$ phase in the NiFe$_2$O$_4$ ferrite evidenced during the annealing process is demonstrated in structural and magnetic studies. The analysis of saturation magnetization pointed to the spin canting phenomenon in the surface layer with a slight change of the so-called dead layer upon heating. The room temperature superparamagnetic state (SPM) is modified in the NiFe$_2$O$_4$ sample across annealing as an effect of ferrite crystallization and grain growth as well as hematite separation. For as-received NiFe$_2$O$_4$, with temperature decrease, the blocking process preceded by the freezing process is observed. The silica shell is recognized as the sustaining cover for the SPM state. The electronic structure studies confirmed the complex nature of the Fe-based states.

A. BAJOREK is with the A. Chełkowski Institute of Physics, University of Silesia in Katowice, 75 Pułku Piechoty 1, 41-500 Chorzów, Poland and also with the Silesian Center for Education and Interdisciplinary Research, University of Silesia in Katowice, 75 Pułku Piechoty 1A, 41-500 Chorzów, Poland. Contact e-mail: anna.bajorek@us.edu.pl C. BERGER is with the Université François-Rabelais, Greman, UMR 7347, 16 rue Pierre et Marie Curie, 31071 Tours, France. M. DULSKI, M. ZUBKO and K. PRUSIK are with the Silesian Center for Education and Interdisciplinary Research, University of Silesia in Katowice and also with the Institute of Materials Science, University of Silesia in Katowice, 75 Pułku Piechoty 1A, 41-500 Chorzów, Poland. S. LEWIŃSKA and A. ŚLAWSKA-WANIEWS-KA are with the Institute of Physics, Polish Academy of Sciences, Al. Lotników 32/46, 02-668, Warsaw, Poland. F. GRASSET is with the Univ Rennes, CNRS, ISCR (Institut des Sciences Chimiques de Rennes) – UMR 6226, 35000 Rennes, France. N. RANDRIANANTOANDRO is with the l'Institut des Molécules et Matériaux du Mans UMR CNRS 6283, Le Mans Université, Avenue Olivier Messiaen, 72085 Le Mans, Cedex 9, France.

I. INTRODUCTION

ULTRAFINE spinel nickel ferrite nanoparticles (SF-NPs) adopting the general Ni^{2+}Fe$_2^{3+}$O$_4$ formula[1–17] have been widely studied over the years as materials that can be used for various potential technological applications, *e.g.*, as memory and energy storage devices, permanent magnets, power transformers, telecommunications devices and magnetic fluids as well as having photocatalytic and biomedical applications, *e.g.*, as targeted drug delivery, hyperthermia or cancer treatment.[1,2,16] Among various spinel nanoferrite types, nickel ferrite is one of the most versatile because of its magnetic properties, catalytic behavior, chemical stability, low conductivity, high electrochemical stability and relatively low cost.[1–34] NiFe$_2$O$_4$ nanoparticles were also tested as highly reproducible gas and humidity sensors and as microwave devices.[1] The variety of SF-NP technological applications usually depends on synthesis types, *e.g.*, sol–gel, co-precipitation, microemulsion, combustion, hydrothermal and citrate ball-milling.[1–17] Most applications require a coating of SF-NPs by nonmagnetic and biologically compatible coaters. Such

a process is also suitable for the prevention of particle aggregation. So far, several types of SF-NPs have been prepared as nanocomposites by using silica as a non-magnetic matrix that enables receiving dispersed fine nanoparticles with a narrow size distribution. As reported, a sol–gel method was predominantly applied in preparing such nanocomposites based on, *e.g.*, $NiFe_2O_4$, $CoFe_2O_4$, $CuFe_2O_4$, $ZnFe_2O_4$, $(NiZn)Fe_2O_4$ and SiO_2 matrix.[35–45] One of the positive features of the sol–gel method is the homogeneous dispersion of NPs. Beyond preventing particle aggregation, the silica matrix is used in active catalytic applications, whereas a porous shell allows the transport of gases from and to the ferrite core.

Furthermore, the core/shell structure enhances the thermal and chemical stability of magnetic nanoparticles, which provides a chemically inert surface allowing for its further functionalization. The stabilizing role of the silica shell is protecting the metallic core from any modification or degradation during subsequent heat treatment. In this way, the properties of the obtained compounds can be modified by annealing, which is a key factor for the control tailoring of the structural and magnetic properties. Over the past few years, several studies have been done on $NiFe_2O_4@SiO_2$ nanoparticles synthesized mainly by sol–gel or ball-milling.[35–45] Mitra *et al.*[39] for $NiFe_2O_4$ NPs showed that the duration of heat treatment at different temperatures determines the particle size ≤ 25 nm. However, the superparamagnetic behavior dependent on the NPs size, in this case, was evidenced only at room temperature for particles < 10 nm.

In contrast, Chaudhuri *et al.*[36] discovered SPM behavior for slightly larger and uncoated $NiFe_2O_4$ particles having a size < 15 nm. The influence of the nanoparticle processing on the particle size was proved by Gharagozlou *et al.*,[41] who showed that the silica matrix is the ideal nucleation environment to confine NPs in $x(NiFe_2O_4)/(100-x)SiO_2$ ($10 \leq x \leq 60$ wt pct). The performed research shows that the particle size increases with the annealing temperature (T_A) and the nickel ferrite quantity. In addition, the diamagnetic SiO_2 shell has a noticeable impact on magnetic properties, causing the reduction of magnetization. Shukla *et al.*[37] revealed that the shape of $NiFe_2O_4@SiO_2$ nanoparticles, *e.g.*, nanosphere and nanorod, depends on the applied synthesis route; thus, it affects the shape anisotropy.

Moreover, the performed nitrogen desorption experiments showed that the silica shell is porous with about 3.7 nm size of pores regardless of NPs shape. As demonstrated, the used coatings stabilize the ferrite structure in the particle core against reduction to α-Fe_2O_3 and preserve Ni sites at the surface, which determines the magnetic properties significantly. Wang *et al.*[38] tested $NiFe_2O_4$ ferrites having 6–40 nm grain size and dispersed in 30 wt pct SiO_2. The applied controlled increase of annealing temperature from 800 °C to 1200 °C had a direct impact on the slight increase of (i) the lattice constant, (ii) the coercivity from 23.4 to 179 Oe and (iii) the saturation magnetization from 8.2 to 29.3 emu/g. The evident enhancement of the saturation magnetization was explained as an effect of a dead layer

estimated as 0.76 ± 0.03 nm at the surface of $NiFe_2O_4$ grains. Furthermore, the noticed evolution from SPM (critical size of 10 nm) to magnetically ordered state is induced by the crystallization process as a direct effect of the heat treatment.[38] The core-shell $NiFe_2O_4@SiO_2$ nanocomposites were also used by *Balamurugan et al.*[40] to synthesize aerogels based on a different amount of core-shell structure amorphous Li_2O (LNS) to enhance the supercapacitor performance correlated to the conductivity enhancement.

Thereafter, Umut *et al.*[35] studied the $NiFe_2O_4@SiO_2$ compounds with identical magnetic cores of about 5.83 ± 0.79 nm and two different silica shells of 9.7 ± 1.40 and 12.45 ± 0.95 nm. Both powdered samples were heated under N_2 conditions from room temperature up to 900 °C with 10 °C/min speed. The authors proved that increasing the size of silica coating leads to (i) diminish dipolar interactions, (ii) enhancement of spin disorder at the $NiFe_2O_4$ surface due to broken super-exchange interactions among magnetic ions and (iii) spin canting phenomenon at the $NiFe_2O_4$–SiO_2 interface evidenced by magnetic as well as Mössbauer studies.

Nonetheless, despite the variety of research published so far for $NiFe_2O_4$ and $NiFe_2O_4@SiO_2$ nanoparticles, there is still a gap, especially concerning structural and electronic structure properties of as-received and annealed samples. Thus, herein we present microstructural and magnetic properties of the $NiFe_2O_4$, which was subsequently used as a base compound for synthesis $NiFe_2O_4@SiO_2$ nanocomposite tuned by heat treatment at selected temperature 1000 °C. We used the co-precipitation method to synthesize the parent compound and microemulsion for nanocomposites. We are focused on a detailed analysis of the change within the crystal structure, microstructure, magnetic properties and electronic structure, where so far the latter has not been explored for nanocomposites and is one element of novelty in the presented work.

II. MATERIALS AND METHODS

A. *Synthesis*

The $NiFe_2O_4$ (NFO) nanoparticles were synthesized by the co-precipitation route while $NiFe_2O_4@SiO_2$ (NFO@SiO_2) by microemulsion from elements having a purity > 99 pct (nickel chloride $NiCl_2$, $6H_2O$ from Wako Laboratory; iron chloride—$FeCl_3$, $6H_2O$, heptane, surfactants (bis(2-ethylhexyl) sulfosuccinate sodium salt (AOT) and polyoxyethylene(4)lauryl ether (Brij^{TM}30) and TEOS from Aldrich Laboratory and ammonia 25 pct from Merck Laboratory).

Metallic salts were weighed in a molar ratio of 1:2 according to the stoichiometric formula. A solution of $NiCl_2$, $6H_2O$ ($M = 237.7$ g/mol, 4.754(1) g) and $FeCl_3$, $6H_2O$ ($M = 270.3$ g/mol, 10.812(1) g), was prepared in 60 mL distilled water. This solution was poured as quickly as possible under vigorous stirring to the hot alkaline solution of NaOH (250 mL to 1 mol/L), which was subsequently heated at 95 °C for 90 minutes and cooled down to the ambient temperature. As already

observed,[46] the temperature significantly accelerates the formation of ferrites, and during the boiling time, dissolution-crystallization processes could occur.

$$1NiCl_2, 6H_2O + 2FeCl_3, 6H_2O + 8NaOH \rightarrow 1\ NiFe_2O_4 + 22H_2O + 8NaCl$$

[1]
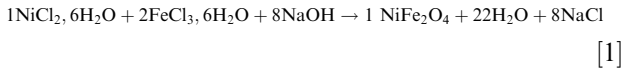
The obtained precipitate was separated from the liquid by a multi-step centrifugation process: (1) separation: 4000 rpm for 10 minutes, (2) washing with distilled water and separation: 4000 rpm for 10 minutes and (3) washing with acetone and separation: 1650 rpm for 10 minutes. The powder was dried in air for 48 hours and kept at room temperature. After this treatment, agglomerates of nanoparticles were obtained.

Then, the nanocomposite NFO@SiO₂ was synthesized based on our previous results on functional silica prepared by the microemulsion process.[47,48] First, a batch of the NFO powder was dispersed into the solution of nitric acid HNO_3 (25 mL to 1 mol/L) for 15 min under vigorous stirring. Such treatment, named peptization, was applied to create a surface charge to promote electrostatic repulsion essential for a ferrofluid synthesis. After adding acetone, the precipitate was once again centrifuged at 4000 rpm for 15 minutes. Double rinsing in acetone was required to eliminate the NO^{3-} charge, which screens the positive charge at the surface of nanoparticles. Afterwards, separation by centrifugation process at 1650 rpm for 10 minutes was applied. The obtained powder was dispersed in distilled water (125 mL) to obtain a ferrofluid. The microemulsion approach used comprises three phases: aqueous phase, oil phase and surfactants. The first-mentioned one contained acidic ferrofluid, TEOS as silica precursor and NH_4OH (28 pct), whose task is to reduce pH of the solution allowing condensation of TEOS after hydrolysis by acidic ferrofluid. The second phase contained heptane. The surfactants used were AOT (13 g) and Brij^{TM} 30 (13.7 mL), where the last-mentioned plays the role of the interface between the two liquid phases. At the beginning of the synthesis process, the solution of heptane, AOT and Brij 30 was prepared in a 250-mL flask.

After 45 minutes of agitation, 3.2 mL of NFO ferrofluid was added. Next, after another 45 minutes of agitation, the 4 mL of TEOS was poured into the mixture. The last 45 minutes of agitation was finished by adding 2.5 mL of ammonia. The obtained mixture was subsequently left to stir for 48 hours. Then, ethanol was added until microemulsion was destabilized. Later, the precipitate was separated by centrifugation at 4000 rpm for 10 minutes and next washed with ethanol by centrifugation at 4000 rpm for 10 minutes. The next step of double washing, this time with acetone, was done by centrifugation at 1650 rpm for 10 minutes. At the last stage of the synthesis, the obtained (NFO@SiO₂) nanopowder was dried in air for 48 hours. Both synthesized samples were studied in the as-received form and after annealing at 1000 °C for 6 hours at the ambient atmosphere.

B. Characterization

The crystal structure was examined by employing X-ray powder diffraction (XRD) using an Empyrean PANalytical diffractometer equipped with Cu X-ray source ($K_{\alpha 1}$ of 1.54056 Å) with the Bragg-Brentano geometry θ to 2θ and PIXcel-3D detector.

Infrared measurements were performed using an Agilent Cary 640 FTIR spectrometer equipped with a standard source and a DTGS Peltier-cooled detector. The spectra were collected using the GladiATR accessory with Ge plate (Pike Technologies) in the 4000–750 cm^{-1} range with a spectral resolution of 4 cm^{-1} and recorded by accumulating 16 scans. The water vapor and carbon dioxide were subtracted from the spectrum, while the baseline correction and peak fitting analysis were performed using the GRAMS 9.2 software package.

The transmission electron microscopy (TEM) studies were performed using Jeol JEM 3010. First, the measured sample suspended in ethanol was placed in the ultrasonic washer for 2 hours to fracture agglomerates. Next, a few suspension drops were placed on the carbon-coated Cu grid (400 mesh). As usual, TEM and HRTEM images were recorded for more than one region of interest (ROI). The scanning electron microscopy (SEM) images were recorded using a Jeol JSM-7100F FEG (field emission gun) microscope operated at 15 kV in secondary electron (SE) mode.

All X-ray photoemission spectroscopy (XPS) results were obtained at room temperature by using monochromatic X-ray source Al K_α (1486.6 eV). The sample was fixed into the sample holder by double-coated conductive carbon tape and subsequently was stored under ultra-high vacuum for a week. Next, the XPS measurement was performed in two consecutive steps. In the first, the as-prepared material was studied directly after its storage (1 step). Afterwards, the same specimen was sputtered by Ar$^+$ ion beam for 30 min (2 step), and then the sample was measured. All the XPS spectra obtained were calibrated using C1s peak (BE = 284.8 eV) as carbon peak, which usually originates from the carbon adsorbed at the surface of the sample and is used as a reference for charge correction. All spectra measured were processed with the use of MultiPak 9.7 software.

The magnetic properties of as-received samples were determined based on wide-range Superconducting Quantum Interference Device (SQUID) magnetometer MPMS XL7 Quantum Design, while a commercial Physical Property Measurement System (PPMS, Quantum Design) with VSM and VSM Oven options was used in magnetic behavior studies of annealed specimens. The thermal dependence of DC magnetization was collected in the zero-field-cooled (ZFC) and field-cooled (FC) modes at the external field of 100 Oe and 1000 Oe, in the temperature range from 2 K to 400 K, while the isothermal magnetic curves M(H) were recorded at 2 K, 100 K, and 300 K.

The Mössbauer spectra collected at a temperature > 77 K were recorded using a standard transmission geometry equipped with a conventional constant accel-

eration spectrometer and a [57]Fe source diffused into an Rh matrix. Every run of measurement took about 24 hours at high temperature and less for low temperature (< 77 K) because of increases of f-factor, favoring the measurement. A spectrum calibration was made with pure α-Fe powder.

III. RESULTS AND DISCUSSION

A. *XRD*

The spinel ferrite nanoparticles (SF-NPs) crystallize in the cubic structure, which may have two forms: normal or inverse, depending on A^{2+} and B^{3+} cation distributions over (16d) octahedral or (8a) tetrahedral sites. In the first, (AB_2O_4), the Fe^{3+} cations are only located in the octahedral site as follows $[A^{2+}]^A[Fe^{3+}]_2^BO_4^{2-}$, while in the second $(B)(AB)O_4$, the trivalent iron cations are moved into the tetrahedral site adopting the formula $[Fe^{3+}]^A[A^{2+}Fe^{3+}]_2^BO_4^{2-}$.[21,28,32] As demonstrated, sometimes, at the nanoscale, the random distribution of divalent and trivalent cations between A and B sites depends on the used synthesis process.[28] The NFO nanoferrites crystallize in the inverse spinel ferrite structure in the following formula $[Ni_{1-x}^{2+} Fe_x^{3+}]^A[Ni_x^{2+} Fe_{2-x}^{3+}]^BO_4^{2-}$,[17,27,32] where generally $x = 1.0$ and the occupation within (A) tetrahedral and (B) octahedral sites may be assigned as A = Fe and B = NiFe.[28]

The XRD patterns for as-received and annealed NFO and NFO@SiO$_2$ samples are presented in Figure 1. Both patterns indicate that as-received and annealed samples crystallize in the cubic inverse spinel structure with the $Fd\overline{3}m$ space group. As one may notice for as-received NFO nanoparticles, the diffraction peaks are broadened, indicating the ultrafine crystal structure. The average crystallite size was determined based on the Scherrer formula:

$$d_{cryst}^{XRD} = \frac{K\lambda}{\beta\cos\theta} \qquad [2]$$

where: (i) K is the Scherrer constant which for a spherical particle equals 0.89; (ii) λ is the incident X-ray (here Cu K$_\alpha$ line); (iii) $\beta = \sqrt{\beta_m^2 - \beta_s^2}$ is the full width at half-maximum (FWHM) containing the experimental β_m and the β_S = 0.08 instrumental line broadening determined from the standard silicon sample; (iv) θ is the diffraction angle corresponding to the most intense (311) peak in the inverse spinel structure. The result obtained for as-received NFO nanoparticles is very rough due to overlapping (311) and (200) peaks. Nonetheless, it gives the approximate result of d_{crys} = 2.1 ± 0.8 nm. Diffraction peaks become sharp and narrower for annealed specimens due to the crystallinity enhancement induced by the heat treatment (top of Figure 1(a)). The structural Rietveld refinement was performed for the annealed NFO sample based on the NiFe$_2$O$_4$ structure (ICSD 01-074-2081). The refinement procedure was done by considering the additional phase, which emerged during the annealing process. The low values of refinement factors point to using an appropriate refinement procedure. All the values estimated based on the refinement are presented in Table I. As was shown, the additional peaks observed in the diffraction pattern are indexed with rhombohedral hematite α-Fe$_2$O$_3$ with the space group R-$3c$ (ICSD 04-008-7622). The refinement procedure using Pseudo–Voigt 2 function allows estimating the percentage amount of NFO phase as about 52 pct and α-Fe$_2$O$_3$ phase as 48 pct. Similarly, the refined value of crystallite size equals d_{crys} = 57.7 ± 3.1 nm and d_{crys} = 90.7 ± 4.4 nm, respectively. Such secondary phase was already noted for ferrites, *e.g.*, by Huo et al.,[4] Shukla et al.[37] and Pozo Lopez et al.[42,43] as a result of synthesis and further processing.

The XRD patterns for as-received and annealed NFO@SiO$_2$ samples are depicted in Figure 1(b). For the as-received sample, the XRD pattern contains diffraction lines specific to the tetragonal SiO$_2$ structure (space group $P41212$) (ICSD 04-002-8512). However, all the observed lines are very broad as for the amorphous material. The whole XRD spectrum is dominated by the broad peak observed between 15 and 35 deg (see inset in Figure 1(b)), being direct evidence that this material is mainly dominated by the amorphous silica matrix as evidenced by TEM studies. If there is a trace of crystalline NFO nanoparticles, it is rather covered by SiO$_2$, and the (311) peak of the NFO phase is hidden in the background. Similar behavior was already observed by, *e.g.*, Gharagozlou,[41] Balamurugan et al.[39] Mitra et al.[39] and Pozo Lopez et al.[42]

After annealing, the SiO$_2$ crystallized in the monoclinic Aa structure (ICSD 04-012-1134) with refined lattice parameters a = 25.9367(4) Å, b = 5.0012(6) Å, c = 18.4720(2) Å and angle β = 117.4601(3) deg. For this structure, peaks with the highest intensity were marked in Figure 1(b). Based on the refinement procedure, the size of crystallites of SiO$_2$ was determined as 76.7 ± 13.5 nm and the lattice strain as (3.6 ± 1.8) × 10^{-3}. The refinement factors equal, respectively, R_p = 4.32 pct, R_{wp} = 6.78 pct and R_{exp} = 6.19 pct. There is no evidence of the NFO cubic structure nucleation in the silica matrix by analyzing the XRD pattern.

B. *FTIR*

A reference spectrum of NiFe$_2$O$_4$ was measured and analyzed more in detail to correctly interpret the structural properties of the composite systems, *i.e.*, spinel embedded into the silica. According to the infrared data, the region below 750 cm^{-1} is defined by overlapping bands associated with the spinel ferrite[49] and iron oxides. Unfortunately, due to the limitation of the detector and type of Ge crystal taken into the analysis, there is no possibility to analyze central structural units characteristic for the spinel structure. Other bands of the low-wavenumber region are problematic in the interpretation and might be explained as two-fold. According to the literature, those bands may result from the iron oxide impurities such as a poorly crystalline iron hydroxide,[50–54] amorphous goethite[55] or defective hematite (proto/hydrohematite).[55–57] An-
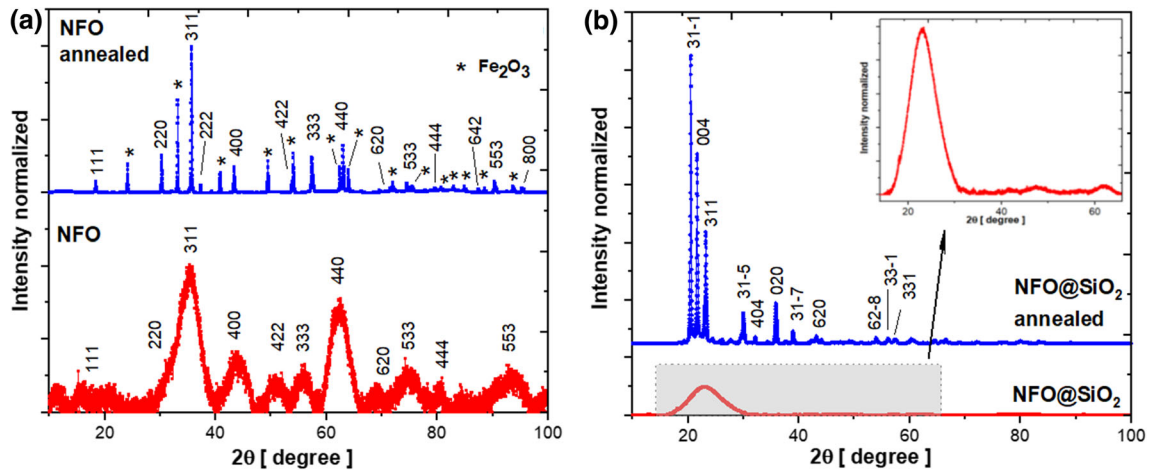
Fig. 1—XRD pattern for as-received and annealed (a) NFO and (b) NFO@SiO$_2$ specimens.

Table I. Refined Crystal Structure Parameters for the Spinel Ferrite NFO Annealed Nanopowder

NFO Annealed		Phase NiFe$_2$O$_4$ Cubic *Fd-3m*				Phase α-Fe$_2$O$_3$ Rhombohedral *R-3c*				
Lattice Parameters (Å)		$a = 8.3377$				$a = 5.0359$ $c = 13.7424$				
Crystallite Size (nm)		57.7 ± 3.1				90.7 ± 4.4				
Lattice Strain ε_{RMS}		$(11.36 \pm 0.37) \times 10^{-4}$				$(2.27 \pm 0.31) \times 10^{-4}$				
Occupation		*x*	*y*	*z*	Occ.		*x*	*y*	*z*	Occ.
	Fe (8a)	0	0	0	0.5071	Fe (12c)	0	0	0.6478	1.0
	Ni(16d)	0.625	0.625	0.625	0.5148	O (18e)	0.3061	0	0.25	1.0
	Fe(16d)	0.625	0.625	0.625	0.5148					
	O (32e)	0.868	0.868	0.868	1.0					
Refinement Factors	$R_{exp} = 6.38$ pct $R_{wp} = 2.52$ pct $R_p = 1.36$ pct									

other hypothesis may refer to the presence of hydroxyl/water impurities adsorbed at the hematite surface or incorporated into the spinel ferrite structure. In turn, the interpretation of three bands centered at around 820, 917 and 1022 cm^{-1} is sightly problematic, and their understanding may be associated with the deformation modes of lattice hydroxyl "defects" or δ(OH) of terminal hydroxyl groups (Fe–OH) localized at the hematite surface or within the spinel ferrite structure.[58] It is also worth noting that the band nature of the low-wavenumber region finds confirmation in the analysis of the bands, strong in intensity, localized in the 1200 to 1600 cm^{-1} and 2450 to 3800 cm^{-1} regions. These two regions correspond to the deformational modes and symmetric and asymmetric stretching vibration of water due to the unsaturated surface Fe atoms[59] and hydroxyl units. In turn, the lack of bands of the 1200 to 1600 cm^{-1} and 2450 to 3800 cm^{-1} regions of the infrared spectra of thermally treated ferrites resulted from their fully dehydroxylation and dehydration. In addition, two bands characterized by the full width at half maximum centered at 975 and 1116 cm^{-1} corresponded to nonstoichiometric hematite. Unfortunately, there is no possibility to follow the structural modification of the nickel

ferrite particles due to the detector limitation and Ge plate.

The spectrum of as-synthesized composite, spinel and silica is dominated mainly by absorption bands of the 750 to 1300 cm^{-1} region (see Figure 2) originated from modes of Si–O–Si and O–Si–O.[60] A band centered at 950 cm^{-1} may be correlated with the Si–OH bond[60] or the presence of the nonstoichiometric fragments of the silicon oxide network.[61] Unfortunately, there is no possibility to easily recognize bands linked to the spinel because of the robust signal of silica in the low-wavenumber region. As a result, the evidence of iron ferrite in the composite provided only band analysis of the 1300 to 3800 cm^{-1} area. A similar band arrangement for the number and intensity was also observed in the composite spectrum as for the reference NFO spectrum. It may indirectly suggest the presence of water molecules anchored to the surface of the spinel nanoparticles. However, it is worth keeping in mind that some of the bands stronger in intensity, especially around 1600 cm^{-1}, resulted rather from water molecules or hydroxyl groups anchored to the surface of the silica. Unfortunately, the 3200 to 3800 cm^{-1} range is also slightly problematic in the interpretation because of overlapping signals of v(Si–

OH) as well as ν(OH) and molecular water adsorbed at both silica[62] and spinel nanoparticle surfaces.

An infrared spectrum of the sintering composite turned to be much more unambiguously in the interpretation, especially in the context of the spinel nanoparticl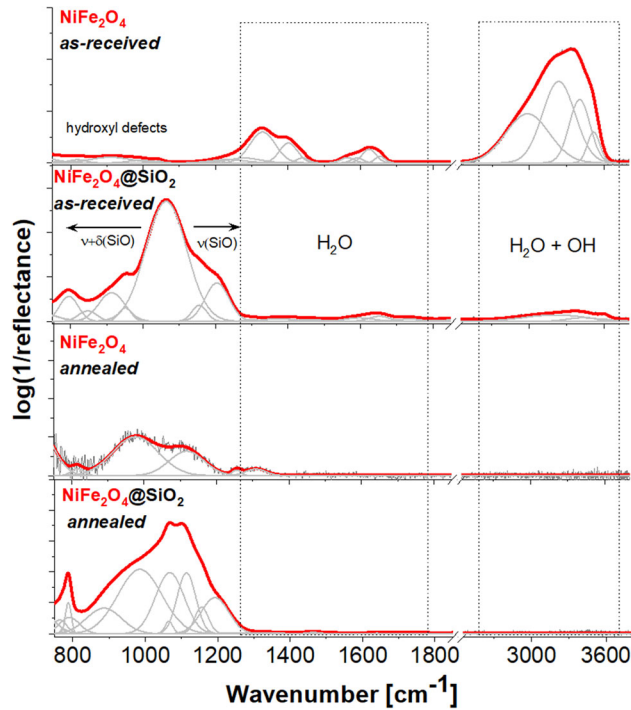es or non-sintered system. Silica bands of the 750 to 1300 cm^{-1} region are still very strong in intensity (see Figure 2). Moreover, the deconvolution procedure and peak fitting analysis revealed the crystallization of initially amorphous silica, and the band arrangement suggests the formation of cristobalite.[63,64] In turn, the applied thermal conditions provided the visible weakening of the other bands, especially considering the water molecules and hydroxyl units, compared to the initial material. Unfortunately, this observation practically eliminates the possibility of interpretation of the spinel nanoparticles in the sample. As a result, other techniques are needed to follow the structural parameters and describe chemical information about the spinel ferrite.

C. Microstructure—TEM and SEM

The TEM micrographs of as-received pristine NFO particles and those coated by silica are depicted in Figures 3 and 4. The first analyzed TEM image, acquired in a bright field (BF) (see Figure 3(a)), displays the presence of small NFO particles. The selected area electron diffraction (SAED) pattern in the left corner indicates the nanoscale crystallinity with randomly oriented polycrystalline grains having an inverse spinel symmetry. The crystallite size statistical distribution (CSD) histogram of about 100 grains was estimated based on a dark-field (DF) image depicted as a bottom inset in Figure 3(b). As shown, the average particle size estimated based on statistical log-normal function

$$P(D) = \frac{A}{D\,\sigma_D\,\sqrt{2\pi}} \exp\left[-\frac{1}{2\,\sigma_D^2} \ln\left(\frac{D}{d_p}\right)^2\right] \quad [3]$$

where σ_D denotes the standard deviation of the average particle size d_p, which equals $d_p \sim 3.7$ nm $\pm$ 0.3 nm with

Fig. 2—Infrared spectra of reference nickel ferrite nanoparticles and particles embedded into the silica before and after sintering at 1000 °C. The characteristic bands originated from vibrational modes of central structural units of spinel and silica are highlighted by arrows.
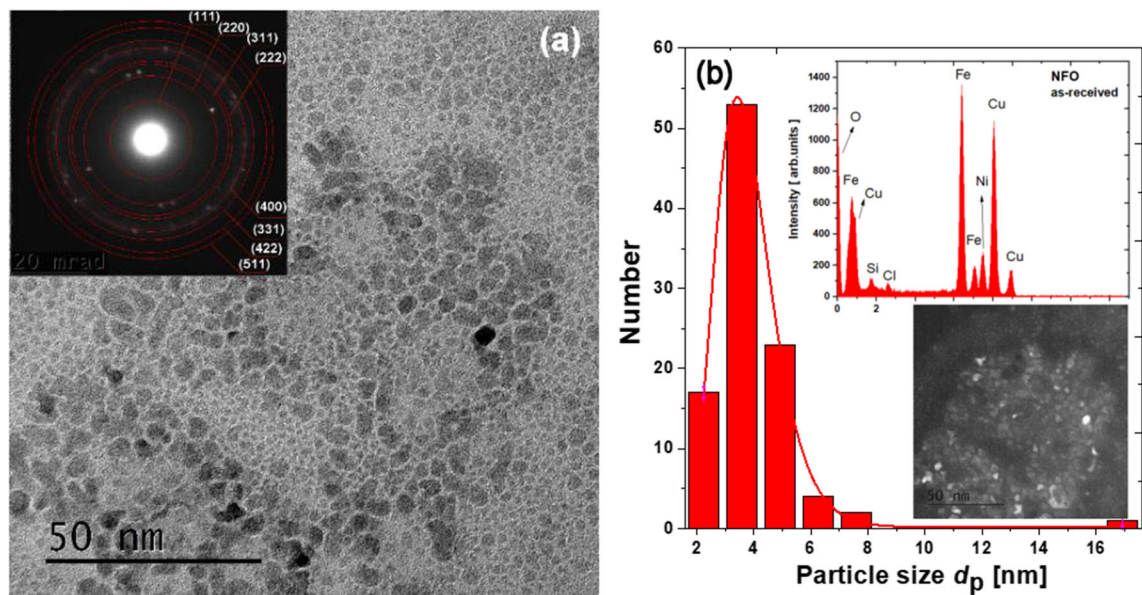

Fig. 3—TEM micrographs for pristine NFO particles: (a) bright-field image; (b) crystallite size distribution (CSD). As bottom inset, the dark-field image and upper-left corner EDS analysis were performed for the region of interest depicted in the dark-field image.
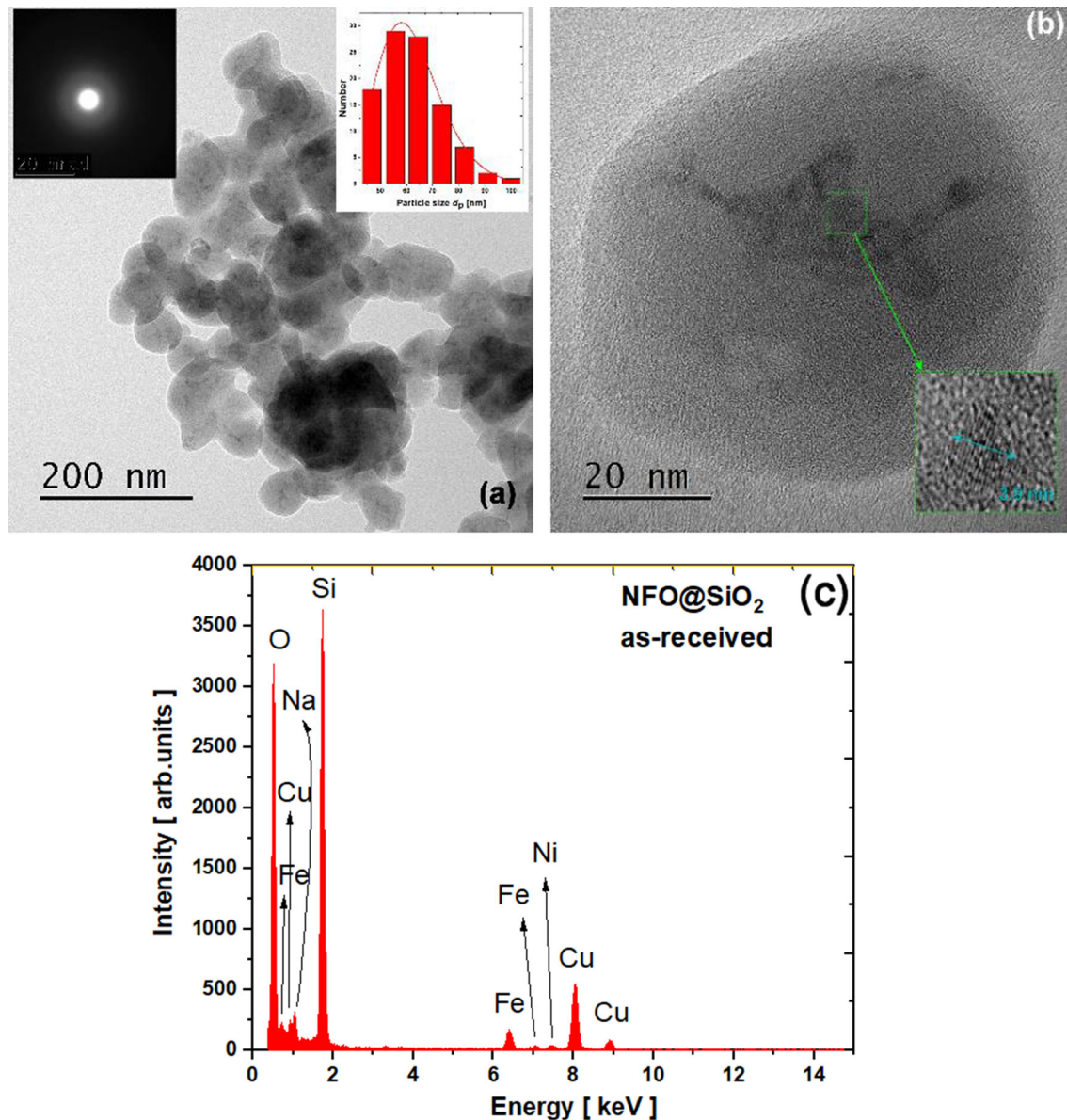
Fig. 4—TEM micrographs for as-received NFO@SiO$_2$ particles: (*a*) bright-field image with SAED as a left inset and crystallite size distribution (CSD) as a right inset. (*b*) HR-TEM bright-field image of a single NFO@SiO$_2$ particle with visible NFO clusters composed of single NFO particles (bottom inset); (*c*) EDS spectrum.

the minimum size of 2.3 nm and maximum size of 18.3 nm. The obtained results are consistent with XRD data. The EDS spectrum confirmed the presence of the NFO phase.

The microstructural analysis of NFO encapsulated into silica matrix shows that as-received particles are almost spherical, but the core-shell structure is hardly noticed (see Figure 4(a)). Instead of such a system, the irregular distribution of NFO clusters inside SiO$_2$ is evident, especially in the HR-TEM image (see Figure 4 (b)). The analysis of these clusters performed based on their distribution inside the NFO@SiO$_2$ composite allowed us to determine the average size of NFO nanoparticles, estimated as $d_p \sim 3.9 \pm 0.5$ nm. The example of such an individual particle is depicted as a bottom inset in Figure 4(b). The SAED placed as an inset in Figure 4(a) is rather typical for amorphous materials, and we infer that the SiO$_2$ matrix is amorphous. The particle size distribution analysis performed based on Figure 4(a) allowed for an estimation of NFO@SiO$_2$ diameters. The average diameter was determined as $d_p \sim 60.5 \pm 0.5$ nm by using the log-normal function. The EDS analysis (see Figure 4(c)) reveals peaks typical for NFO structure dominated by Si (from SiO$_2$) and Cu (from the copper grid). A slight impurity trace of Na as a residual element from the synthesis process (AOT) is also noticeable. It is worth mentioning that the disordered layer of NPs surface was estimated as about 0.6 nm for both as-received samples based on TEM images analysis.
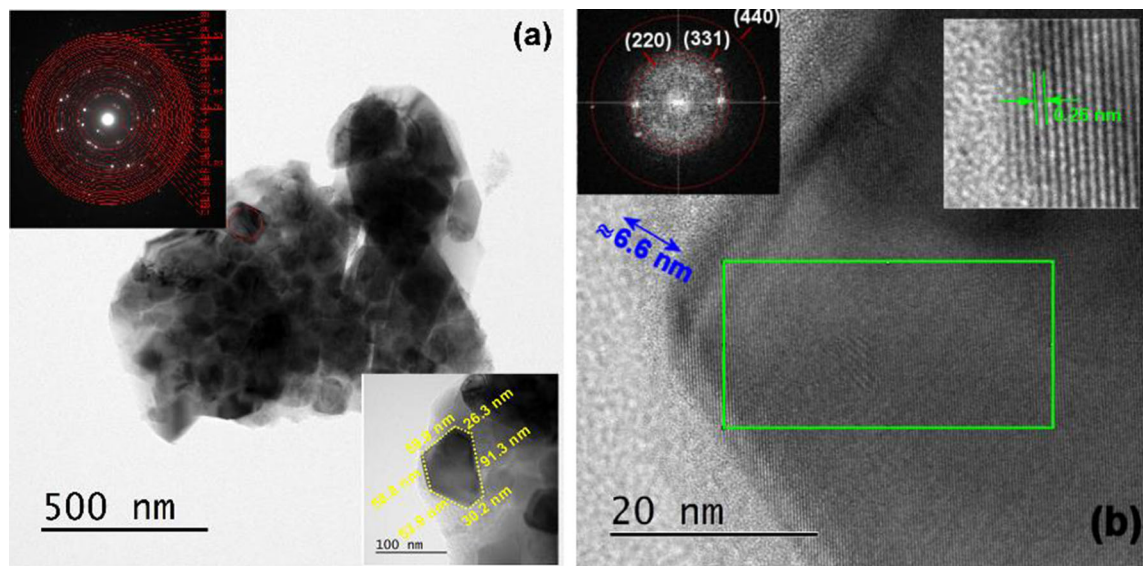
Fig. 5—TEM micrographs for annealed NFO particles: (*a*) bright-field image with SAED as an upper inset and magnified shape of a single particle as bottom inset; (*b*) HR-TEM bright-field image with a visible sharp edge of a single particle. The left inset represents the FFT pattern, and the right inset shows an estimation of interplanar spacing; (*c*) crystallite size distribution (CSD) and EDS spectrum performed for the region of interest depicted in (a) marked by a red circle (Color figure online).

After the annealing procedure, the microstructure of both samples has been significantly changed. In the case of NFO, one can distinguish well-crystallized nanoparticles (see Figure 5(a)) having the average size of $d_p \sim$ 71.7 nm $\pm$ 0.6 (see Figure 5(c)). The particle shape can be approximated by polygons (see bottom inset in the inset in Figure 5(a)), where all edge lengths are marked. The SAED pattern (see upper inset in Figure 5(a)) is typical for the nanoscale polycrystalline inverse spinel structure as the dominated one.

The HR-TEM image taken from one of many crystallites allows for estimating the interplanar spacing of 0.26 nm between adjacent planes, corresponding to (311) lattice plane (see upper-right inset in Figure 5(b)). The FFT analysis performed for the region of interest,

marked with a green rectangle, is indexed to face-centered regular $NiFe_2O_4$ phase along $<111>$ axis. The energy-dispersive spectrum (EDS) registered from the area marked by a red circle in Figure 5(a) reveals elements typical for the NFO phase.

The drastic change in morphology compared to as-received powder is observed for the annealed NFO@-SiO_2 sample (see Figure 6(a)). Here, regular spherically shaped particles wholly disappeared, and instead, relatively thin irregular flakes dominated by crystallized SiO_2 have emerged. The SAED pattern collected from particles visible in Figure 6(a) is indexed by the monoclinic silicon oxide structure in the zone axis [0-10] (inset in Figure 6(a)), whose presence was confirmed by XRD refinement. However, the EDS spectrum
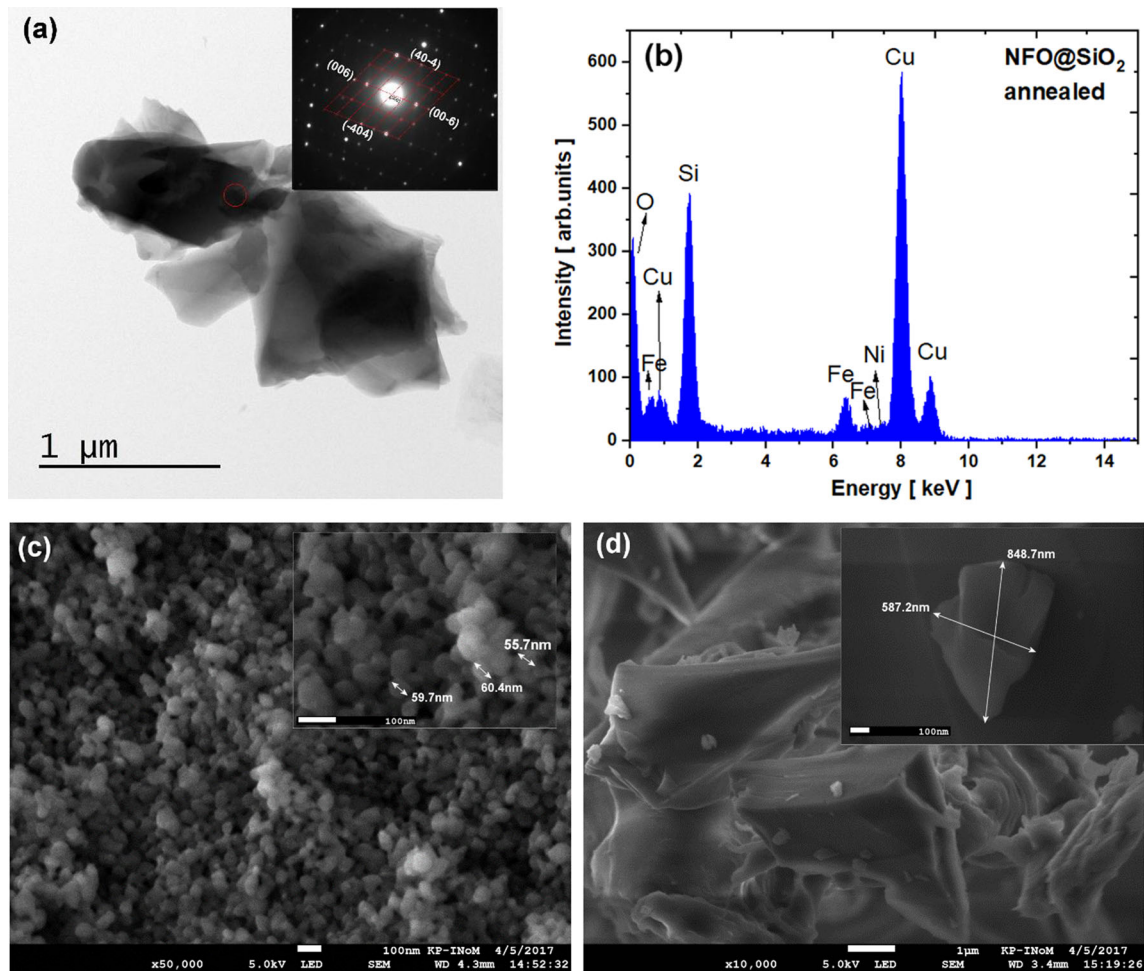
Fig. 6—(*a*) Bright-field TEM micrograph for annealed NFO@SiO₂ sample. Insert represents SAED pattern; (*b*) EDS spectrum performed for the region of interest marked with a red circle in (a) image. SEM images for (*c*) as received and (*d*) annealed NFO@SiO₂ samples. In both inserts, the smallest observed particles are depicted.

presented in Figure 6(b), recorded from the area marked with a red circle in Figure 6(a) reveals the presence of Si element as a representative of SiO_2 and features typical for the NFO phase. Nonetheless, the intensity of the latter ones is relatively low compared to SiO_2, which is in good agreement with other performed studies. Figures 6 (c) and (d) represent SEM images for the NFO@SiO₂ sample for its as-received and annealed form, respectively. The as-received sample has a porous structure, and the formation of multigrain agglomerations consisting of fine crystallites is noticeable. The variation with morphology induced by the heat treatment is evident. The most miniature observed objects vary by about an order of magnitude (see both inserts), consistent with XRD and TEM studies.

D. *Magnetic Properties*

1. *FC-ZFC magnetization*

The temperature DC magnetization studies were performed for both as-received samples, in the zero-field-cooled (ZFC) and the field-cooled (FC) modes and at the external magnetic field of 100 Oe and 1000 Oe (see

Figures 7(a) and (b)). Notably, the ZFC dependences exhibit a quite sharp peak at the maximum temperature, T_{max}, typical for superparamagnetic or spin glass systems. The sharp nature of the observed maxima is associated with a relatively narrow distribution of particle sizes in these two samples proved by TEM studies.

In the case of NFO nanoparticles, the value of $T_{max} \approx$ 32.5 K $\pm$ 5 K (100 Oe) and $T_{max} \approx$ 37.5 K $\pm$ 5 K (1000 Oe) and the reversibility of ZFC-FC curves from T_{max} to 400 K are very well observed. Such overlapping of ZFC-FC curves, also in the region of the maximum, and the shape of the FC curve below T_{max} are typical for interacting nanoparticle systems and reflect a collective freezing process in this sample.[65] Collective behavior in as-received NFO nanoparticles also was proved by TEM studies, where rather agglomerated grains are visible; thus, interactions between them could not be excluded. Nevertheless, to confirm the assumption about the frozen state in the as-received NFO sample, further AC magnetization studies should be performed. Attention should also be given to a hump visible in the low-temperature part (between 5 K and 10 K) of the
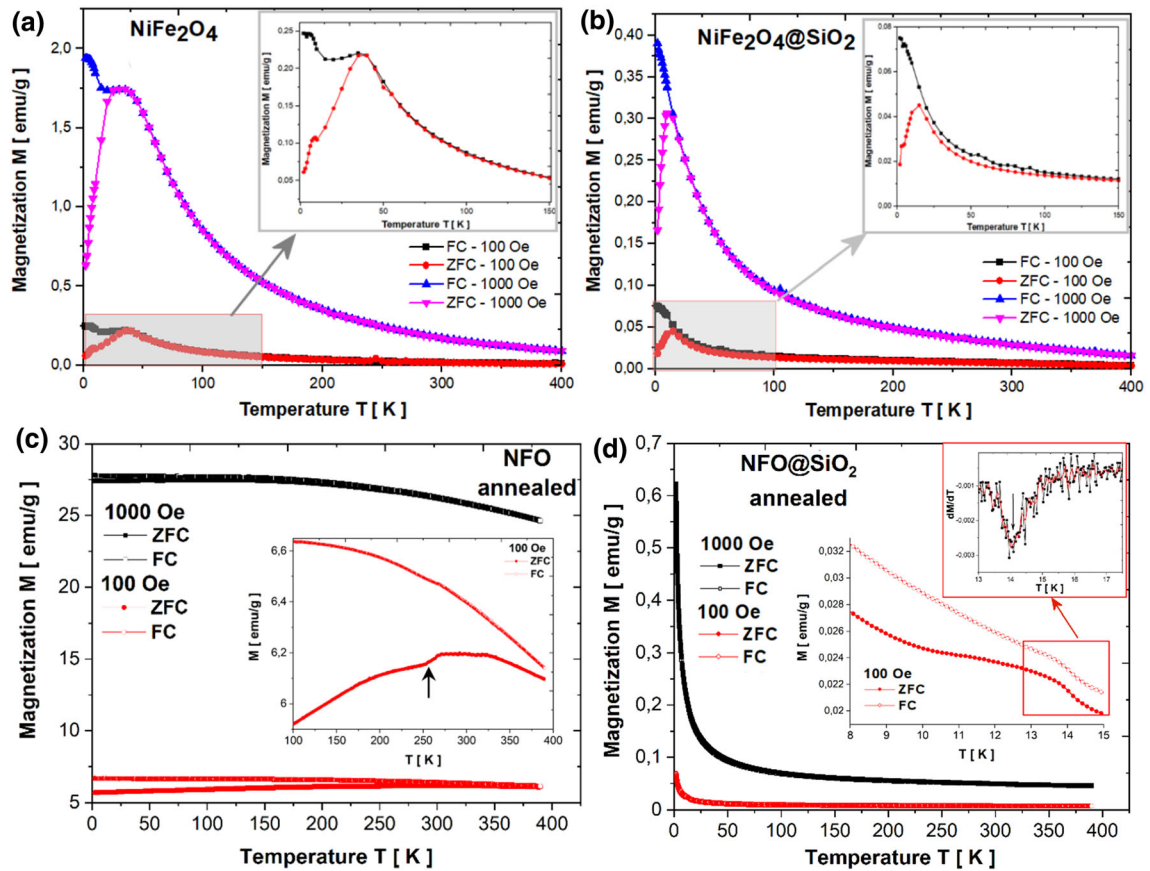
Fig. 7—Temperature dependences of DC magnetization measured at 100 Oe and 1000 Oe for as-received (*a*) and (*b*), as well as annealed (*c*) and (*d*), NFO and NFO@SiO₂ specimens, respectively.

ZFC curve measured at 100 Oe. This broad anomaly is most likely related to a blocking process of some non-interacting particles also present in the NFO sample. It means that, with the temperature decrease, the freezing process is observed before the blocking process–it should be emphasized here that such behavior is rarely described in the literature.[65]

For the composite NFO@SiO₂ specimen, the ZFC maximum is observed at $T_{max} \approx 14.8$ K $\pm$ 5 K (100 Oe) and $T_{max} \approx 11.9$ K $\pm$ 5 K (1000 Oe), where T_{max} rather expresses the blocking temperature. Also, the shape of the FC curve in the irreversibility region (the sharp increase of the magnetization with the temperature decrease) is specific for the blocking process.[66] Considering that, investigated here, NFO particles are well dispersed in the silica matrix, the interaction between them is negligible; thus, the blocking process seems to be obvious, and T_{max} can be treated as a blocking temperature. What should be stressed is that such values of T_{max} are demonstrated for non-annealed NFO@SiO₂ nanocomposites for the first time to our knowledge.

The ZFC-FC dependences for annealed specimens are shown in Figures 7(c) and (d). The annealing process changed the morphology and structure of the samples confirmed by the TEM and XRD results; thus, the comparison of magnetic properties between as-received and annealed samples became impossible. From TEM

results (see Figure 5), we know that the annealed NFO sample consists of large crystalline grains, most likely welded to each other, so any blocking or freezing processes are excluded. Therefore, the ZFC-FC relations plotted in Figure 7(c) present an irreversible process of magnetizing such a system, which can be treated as a bulk magnet. Nonetheless, it should be noted that a kink in the ZFC curve between 250 K and 260 K denotes the Morin transition usually observed in hematite at T~260 K,[67,68] which confirms the presence of this phase in the annealed NFO sample. Figure 7(d) presents ZFC-FC curves for the annealed NFO@SiO₂ sample measured at 100 and 1000 Oe. Both ZFC and FC curves show the magnetization increases with decreasing the temperature as in the paramagnetic system. This behavior indicates the decomposition of ferrite nanoparticles to paramagnetic ions due to the annealing process and what follows the domination of paramagnetic contribution in the annealed NFO@SiO₂ sample. Also, a broad maximum as an inflexion point around $T_{inf} \approx 14 \pm 1$ K estimated from d*M*/d*T* relation placed as an inset in Figure 7(d).

The high-temperature magnetization is only presented for annealed samples because of the low signal for non-annealed ones. For the NFO specimen, a sudden drop in the magnetization value with a temperature > 800 K is related to the magnetic phase transition (see Figure 8 (a)). We determine this temperature to be $T_C \approx 875 \pm 5$
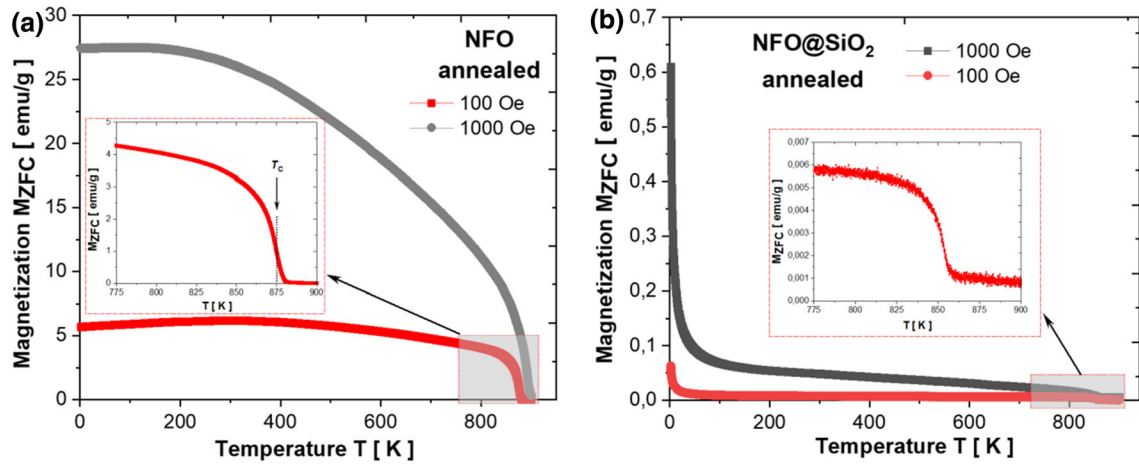
Fig. 8—High-temperature magnetization for annealed (*a*) NFO and (*b*) NFO@SiO$_2$ samples.

K, which is in fair agreement with the bulk NiFe$_2$O$_4$. Previously, Nabyouni *et al.*[22] estimated the Curie temperature from inductance as 517 °C (790 K) for nanocrystalline NFO, whereas for the bulk is 570 °C (843 K). Additionally, it is worth noting that Shafi *et al.*[22] observed similar behavior based on magnetic force measurements by thermogravimetric balance for sonochemically synthesized nanoparticles and demonstrated that the Curie temperature value for the amorphous sample with ultrafine particles equals T_C = 440 ° C (713 K) followed by significantly higher T_C = 560 °C (833 K) noted for the crystalline specimen. The authors claimed that the broad magnetic phase transition could be attributed to the particle size distribution. Both values are lower than noted for bulk material where T_C = 585 °C (858 K). Thus, the evident increase of T_C observed always with the heat treatment is due to the crystallization effect preceded by the presence of ultrafine particles in the studied NFO sample. As the particle size increases, its surface to volume ratio is reduced, which is reflected in fewer atoms on the surface. This behavior is subsequently followed by an enhancement of magnetic ordering, which is manifested as the rise of saturation magnetization and ferrimagnetic T_C ordering temperature. All the factors were observed by us for the NFO sample annealed at 1000 °C for 6 hours compared to the as-received one.

In the case of the NFO@SiO$_2$ specimen (see Figure 8 (b)), the high-temperature magnetization dependence besides the low-temperature paramagnetic signal also revealed the additional phase transition around T_C = 856 ± 5 K, which, based on previous analysis, is ascribed as a trace of the NiFe$_2$O$_4$ phase.

2. Hysteresis loops

The magnetic hysteresis (M–H) loops for both as-received samples measured at 2 K, 100 K and 300 K presented in Figure 9 display the typical thick S-shape as for spinel ferrites.[1,53,54] As one may notice for the as-received samples at low temperature, the observed hysteresis is the effect of the ferrimagnetic alignment between A and B sublattices. At room temperature, the possible existence of superparamagnetic (SPM) behavior

is confirmed by zero coercivity and negligible remanence value (see Figures 9(a) and (b) and Table II). The observed non-saturated hysteretic behavior, as in many other ferrites, is associated with: (i) the possible existence of strong inter-particle interactions and (ii) the presence of small nanoparticles having a so-called core shell-like morphology, with ferrimagnetically or ferromagnetically arranged core and spin-glass-like surface layer pointing to the significant impact of surface anisotropy compared to volume ones.[1]

The magnetic anisotropy constants at different temperatures were estimated from the approach to the saturation region by using the empirical law:

$$M(H) = M_S\left(1 - \frac{a}{\sqrt{H}} - \frac{b}{H^2}\right) + \chi_p H \qquad [4]$$

where $M(H)$ is the magnetization at the external applied magnetic field, and M_S is the saturation magnetization. The $a/\sqrt{H}$ term represents the strain field around dislocations by Brown and nonmagnetic inclusions in voids by Néel[39] associated with point-like defects and intrinsic magnetostatic fluctuations, which both are strongly dependent on particle size in nanocompounds. The second term b/H^2 represents various kinds of anisotropies in the cubic compound, *e.g.*, magnetocrystalline anisotropy, shape anisotropy and strain anisotropy, and is expressed as:

$$b \approx \frac{8}{105}\left(\frac{K_1}{\mu_o M_S}\right)^2 \qquad [5]$$

where K_1 is a component of K_{eff}. The last term $\chi_p H$ represents the magnetic paraproces caused by the partial suppression of spin waves by an external applied magnetic field. The estimated values of M_S, a, b, K_1 and χ_p based on fitting of $M(H)$ curves by using the Eqs. [4] and [5] (see Figure 10) are given in Table II. For the annealed NFO, the magnetic parameters are significantly reduced compared to the as-received sample because of changes within particle sizes and shapes and the separation of hematite induced by crystallization processes. In the case of the annealed NFO@SiO$_2$ composite, the anisotropy parameter is enhanced at 2 K
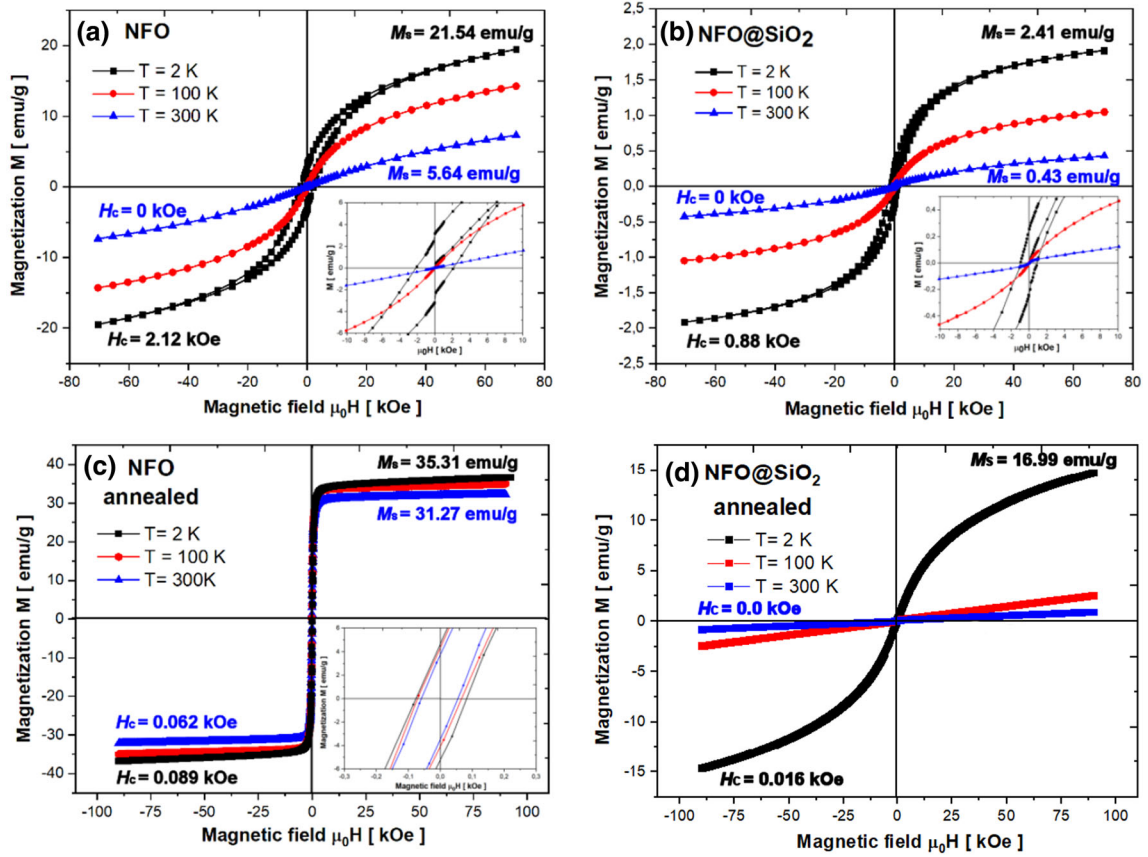
Fig. 9—Hysteresis loops at 2 K, 100 K, and 300 K for as-received, (*a*) NFO and (*b*) NFO@SiO$_2$, and annealed, (*c*) NFO and (*d*), NFO@SiO$_2$ specimens.

but at higher temperatures is reduced compared to as-received samples. The observed phenomenon is associated with the crystallization of silica shell and subsequent modification of NFO particle coating. Mitra *et al.*[39] showed that such parameters determined at room temperature depend on particle size, so M_S is enhanced while K_1 is reduced with the increase of particle size. Similarly, he found that all K_1 values were lower than the corresponding K_{eff} because of the significant influence of surface anisotropy.

Generally, the magnetic properties of nanoferrites are related to the used synthesis route resulting in the occupation of A-tetrahedral and B-octahedral sites by magnetic ions. Thus, the common approach to describing the magnetization process is based on the two—sublattice Néel model,[1,70] where A and B magnetic sublattices are coupled ferrimagnetically by super-exchange interactions. The magnetic M_B and M_A moments may be estimated based on cation distributions and by considering the values of ionic-magnetic moments (Ni^{2+}—2μ_B, Fe^{3+}—5μ_B). So, for the as-received NFO specimen the calculated value $m_{theor} = 2\mu_B$ may differ from its experimental equivalent (m_{exp}) determined from $M(H)$ by the approach to the empirical saturation law (Eq. [4])[39] at room temperature ($m_B = 0.24\ \mu_B$) or 2 K ($m_B = 0.90\mu_B$), respectively. Such discrepancy between experimental and theoretical values originates from the

surface spin disorder, namely, the spin canting effect[1] described by the Yafet–Kittel approach[69–71] based on the three sublattice model. As demonstrated, B (octahedral) sublattice is rather composed of two B1 and B2 sublattices with equal magnitude but oppositely canted magnetic moments with α_{YK} as the canting angle according to the formula:

$$m_{exp}(\mu_B/f.u) = M_B\cos\alpha_{YK} - M_A \quad [6]$$

The estimated α_{YK} value for the as-received NFO compound equals $\approx$ 32.5 deg (2 K) or $\approx$ 41.5 deg (300 K), which is in good agreement with the results previously demonstrated by Šepelák *et al.*[24] and Ahlawat *et al.*[29] based on in-field low-temperature Mössbauer spectroscopy. As the authors noted, the canting angle for a sample with a crystallite size of 9 nm is about 48 deg, which is a bit larger than estimated by *Chinnasamy et al.*[30] for the ball-milled sample with 10-nm-size particles (*i.e.*, $\alpha_{YK} \approx$ 34 deg). The values of the saturation magnetization estimated for NFO nanoparticles are lower those for bulk NiFe$_2$O$_4$ (55 emu/g) compound and other nanoparticles synthesized by different methods, *e.g.*, by mechanosynthesis (M_s = 24.4 emu/g)[24] or modified co-precipitation (M_s = 49.7 emu/g),[35] in our case most likely due to the ultrafine structure of co-precipitated NFO. Thus, the increase of

Table II. Magnetic Parameters for the NFO and NFO@SiO₂ Spinel Nanoferrites

Hysteresis Loop			DC Measurements (100 Oe and 1000 Oe) T_{max} (K)
$T = 2$ K	$T = 100$ K	$T = 300$ K	

NFO As-Received

	$T = 2$ K	$T = 100$ K	$T = 300$ K	
M_S (emu/g)	21.54 ± 0.17	16.14 ± 0.22	5.64 ± 0.27	32.2 ± 5 (100 Oe)
M_S (μ_B/f.u)	0.9	0.69	0.24	
M_R (emu/g)	3.05	0.012	0	37.4 ± 5 (1000 Oe)
H_C (kOe)	2.12	0.015	0	
a ($\sqrt{kOe}$)	2.49 ± 0.02	3.02 ± 0.04	4.07 ± 0.08	
χ_p (emu/g Oe) × 10^{-4}	0.52 ± 0.01	0.48 ± 0.01	0.58 ± 0.02	
K_1 (erg/cm³) × 10^5	3.51 ± 0.05	2.93 ± 0.07	1.32 ± 0.09	

Hysteresis Loops			DC Measurements 100 Oe T_{max} (K)
$T = 2$ K	$T = 100$ K	$T = 300$ K	

NFO Annealed 1000 °C

	$T = 2$ K	$T = 100$ K	$T = 300$ K	
M_S (emu/g)	35.31 ± 0.01	33.39 ± 0.01	31.27 ± 0.01	297 ± 26
M_S (μ_B/f.u)	0.77	0.73	0.68	
M_R (emu/g)	4.66	4.31	2.91	
H_C (kOe)	0.089	0.069	0.062	
a ($\sqrt{kOe}$)	0.078 ± 0.014	0.101 ± 0.009	0.0035 ± 0.001	
χ_p (emu/g Oe) × 10^{-4}	0.19 ± 0.02	0.15 ± 0.001	0.11 ± 0.002	
K_1 (erg/cm³) × 10^5	0.97 ± 0.04	1.95 ± 0.01	1.17 ± 0.01	

Hysteresis Loops			DC Measurements (100 Oe and 1000 Oe) T_{max} (K)
$T = 2$ K	$T = 100$ K	$T = 300$ K	

NFO@SiO₂ As-Received

	$T = 2$ K	$T = 100$ K	$T = 300$ K	
M_S (emu/g)	2.41 ± 0.03	1.32 ± 0.02	0.43 ± 0.02	14.8 ± 5 (100 Oe)
M_S (μ_B/f.u)	0.1	0.06	0.02	
M_R (emu/g)	0.25	0	0	11.9 ± 5 (1000 Oe)
H_C (kOe)	0.88	0	0	
a ($\sqrt{kOe}$)	2.33 ± 0.04	2.98 ± 0.04	3.82 ± 0.09	
χ_p (emu/g Oe) × 10^{-4}	0.016 ± 0.002	0.021 ± 0.001	0.024 ± 0.002	
K_1 (erg/cm³) × 10^5	0.36 ± 0.01	0.25 ± 0.01	0.09 ± 0.01	

Hysteresis Loops			DC Measurements 100 Oe T_{inf} (K)
$T = 2$ K	$T = 100$ K	$T = 300$ K	

NFO@SiO₂ Annealed 1000 °C

	$T = 2$ K	$T = 100$ K	$T = 300$ K	
M_S [emu/g]	16.99 ± 0.04	0.08 ± 0.01	0.06 ± 0.01	14.1 ± 2
M_S (μ_B/f.u)	0.79	0.004	0.002	
M_R (emu/g)	0.011	0	0	
H_C (kOe)	0.016	0	0	
a ($\sqrt{kOe}$)	3.52 ± 0.02	0.85 ± 0.05	0.28 ± 0.02	
χ_p (emu/g Oe) × 10^{-4}	0.38 ± 0.01	0.27 ± 0.01	0.09 ± 0.01	
K_1 (erg/cm³) × 10^5	3.79 ± 0.02	0.009 ± 0.001	0.005 ± 0.001	

M_S is generally thermally induced, and as was shown, the increase of the annealing temperature (T_A) is associated with the enhancement of the crystallization process,[13–24] causing the crystallites/grains growth affecting a decrease of a surface-to-volume fraction.

Comparing the hysteresis loops for as-received and annealed specimens, we can claim that the heat treatment at ambient pressure at $T_A = 1000$ °C has a significant impact on the structure and morphology of the samples, resulting in a change of magnetic properties. The shape of hysteresis loops for the annealed NFO specimen (see Figure 9(a)) is relatively independent of temperature and is typical for spinel soft magnetic material, which confirms that any blocking or freezing process in this sample does not take place. The saturation magnetization of the annealed NFO is equal to 35.3 emu/g at 2 K and 31.3 emu/g at 300 K. The obtained value of the saturation magnetization is consistent with previous research,[4,13,16,18,20,24] where the relation between magnetic properties and crystallization process is evident, and the increase of M_S is linked to the domination of the ordered magnetic moments in the magnetic core of particles. The obtained value of the coercivity and the fact that annealed NFO is
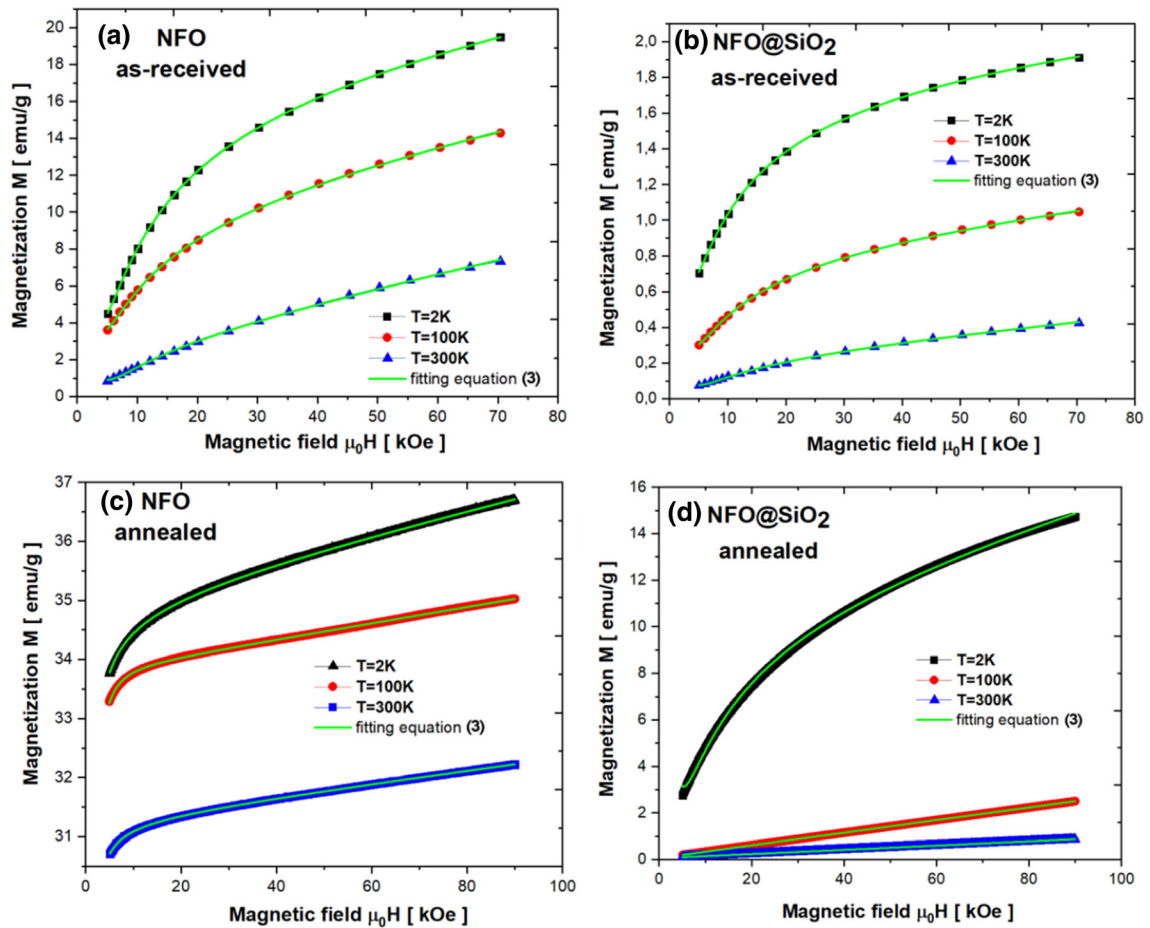
Fig. 10—Fitting of M(H) dependence at 2 K, 100 K, and 300 K for as-received (*a*) NFO and (*b*) NFO@SiO$_2$ and annealed (*c*) NFO and (*d*) NFO@SiO$_2$ specimens based on Eq. [4].

a large grain system suggest that a domain wall motion process dominates the magnetization process. The spin canting phenomenon for the annealed NFO sample is estimated by considering the experimental (m_{exp}) value determined from $M(H)$ curves and the values of ionic-magnetic moments. Additionally, the quantity of the NiFe$_2$O$_4$ phase estimated from XRD as 52 pct was used to correct the m_{exp} values assigned to NFO. Based on the Yafet–Kittel approach, the α_{YK} canting angle is determined as $\alpha_{YK} \approx 34.5$ deg (2 K) or $\alpha_{YK} \approx 35.8$ deg (300 K), which is close to the value for the as-received NFO specimen. On the contrary, for the as-received NFO@SiO$_2$ sample, the surface spin disorder is hard to describe because of the domination of the silica matrix, as shown by TEM studies. The recorded values of the saturation magnetization in emu/g include a contribution from diamagnetic SiO$_2$; hence, these values are small (see Figure 9(b)). Following ZFC-FC results, a small non-zero coercive field at 2 K is related to the blocked state of NFO nanoparticles, and at higher temperatures, the magnetic hysteresis vanishes, pointing to their SPM behavior. At room temperature, M_S is comparable to that previously observed by Chaudhuri et al.,[36] who additionally did not observe any measurable coercivity.

In the case of the annealed NFO@SiO$_2$ sample, we observed the relatively high saturation magnetization at 2 K, *i.e.*, ~17 emu/g, which is nearly seven times higher than for the as-received NFO@SiO$_2$ sample. The TEM and EDS studies of NPs embedded in the silica matrix revealed silica crystallization and the core-shell structure degradation. Also, the EDS analysis demonstrated the presence of submerged NFO in crystallized SiO$_2$. Nevertheless, we cannot exclude that some part of SiO$_2$ burned during the annealing process, and the iron concentration in this sample increased, and, consequently, the drastic increase of M_S value is observed. Similar enhancement (*i.e.*, after annealing process) of M_S was noticed, *e.g.*, by Chaudhuri et al.,[36] Wang et al.[37] and Mitra et al.,[39] but the morphology of their samples is significantly different, so it is hard to compare them to our annealed NFO@SiO$_2$ sample. At 100 K and 300 K, the $M(H)$ dependences are almost linear with zero coercivity as for paramagnetic materials, which confirms the decomposition of some nanoparticles to paramagnetic fractions. The spin canting at the surface layer of NFO coated by SiO$_2$ is assumed by considering the regular distribution of magnetic cations between tetrahedral and octahedral sites as described previously and assuming that the SiO$_2$ matrix is nonmagnetic. So, the
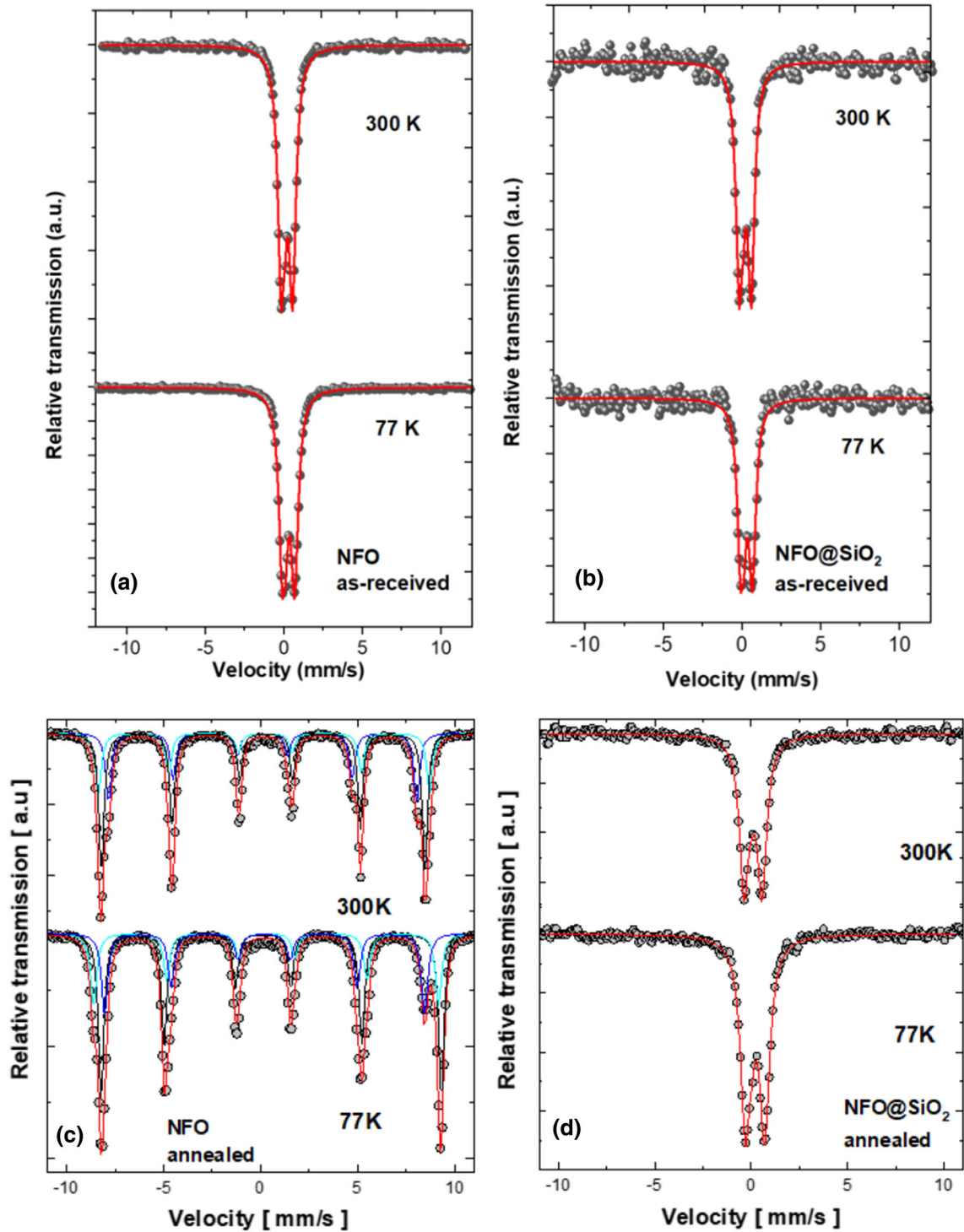
Fig. 11—Mössbauer spectra for as-received (*a*, *b*) NFO and NFO@SiO$_2$ and annealed (*c*, *d*) spinel nanoferrites.

Yafet–Kittel angle α_{YK} between canted spins in B sublattice is determined as $\alpha_{YK} \approx 43.2$ deg (2 K) or $\alpha_{YK} \approx 44.2$ deg (300 K) for as-received NFO@SiO$_2$ composite and $\alpha_{YK} \approx 35.3$ deg (2 K) or $\alpha_{YK} \approx 44.4$ deg (300 K) for the annealed one. The values of the α_{YK} angle determined at room temperature confirm the

sustained magnetic behavior of the surface layer of NFO@SiO$_2$ after annealing.

3. *Mössbauer spectra*
Figure 11 presents Mössbauer spectra recorded at 77 K and 300 K for as-received specimens. By analyzing the

Table III.   Mössbauer Spectra Parameters for the NFO and NFO@SiO$_2$ Spinel Nanoferrites

	IS (mm/s)	QS /2ε (mm/s)	B_{hyp} (T)	FWHM/2 (mm/s)	A (Pct)	Phase
NiFe$_2$O$_4$ As-Received						
300 K	0.32	0.63	—	0.26	100	NiFe$_2$O$_4$
77 K	0.44	0.67	—	0.27	100	
NiFe$_2$O$_4$ Annealed						
300 K						
Site A	0.26	0.00	49.0	0.18	27	NiFe$_2$O$_4$
Site B	0.36	− 0.05	52.7	0.18	24	
	0.37	− 0.16	51.5	0.16	49	α-Fe$_2$O$_3$
77 K						
Site A	0.36	0.02	50.9	0.19	24	NiFe$_2$O$_4$
Site B	0.46	− 0.04	54.9	0.19	28	
	0.50	0.42	54.1	0.17	48	α-Fe$_2$O$_3$
NiFe$_2$O$_4$@SiO$_2$ As-Received						
300 K	0.33	0.65	—	0.25	100	NiFe$_2$O$_4$
77 K	0.43	0.63	—	0.26	100	
NiFe$_2$O$_4$@SiO$_2$ Annealed						
300 K	0.26	0.83	—	0.29	100	NiFe$_2$O$_4$
77 K	0.37	0.88	—	0.32	100	

obtained spectra at room temperature, we may notice a quadrupole doublet typical for the superparamagnetic state present in all measured samples, consistent with the hysteresis loops measurements. The doublet line is preserved on cooling samples to 77 K, meaning that SPM behavior is also observed at this temperature. It is well known that the SPM component in Mössbauer spectra would appear when the relaxation time (τ) of the magnetic moment of nanoparticles is essentially higher than the time measurement (τ_m). For ^{57}Fe Mössbauer spectrometry, the τ_m value is in order of 10^{-8} s. It is also worth mentioning that, as previously reported for spinel nanoferrites, the Mössbauer spectra strictly depend on the chosen synthesis type and further sample processing.[5,16,17,22,24,25,34,35] In the paper of Hoque et al.,[16] the influence of annealing on various physical properties, including the crystallites size of NiFe$_2$O$_4$, is reported. Thus, the approach used by the authors reveals the emergence of a doublet line related to the processing of samples from its as-dried form to annealed up to 400 °C corresponding to the crystallites size from 2 to 4 nm. In our case for the as-received NFO sample with a similar estimated crystallites size, lower than the typical critical size of 10 to 12 nm, we observed the same SPM behavior at room temperature and below. Further heat treatment performed by Hoque et al.[16] leads to gradual crystallization of measured material and emergence of sextet lines in Mössbauer spectra. Similar behavior was also noted by, e.g., Shafi et al.,[22] and Agourianne et al.,[17] who revealed fully sextet components for annealing at higher temperatures up to 1000 °C. After that, Kamzin et al.[34] proved the spin-canting phenomenon in NiFe$_2$O$_4$ nanoparticles synthesized by combining two methods, controllable deposition and hydrothermal synthesis, followed by annealing at 800 °C for 2 hours. Typical sextet structure was evidenced in Mössbauer spectra studied at room temperature without external field and in-field pointing to the presence of canting phenomenon at the surface of NPs due to low surface

symmetry and as a consequence of surface anisotropy or lack of some magnetic Fe ions in the surface layer leading to the frustration effects. The SPM phenomenon was not evidenced because of the significant size of NPs. Later studies performed by Umut et al.[35] revealed a doublet structure at the center of the spectrum, pointing to SPM behavior of narrow size distribution NiFe$_2$O$_4$ nanoparticles with about 6 nm size.

The heat treatment we performed at T_A = 1000 °C for both NFO and NFO@SiO$_2$ samples leads to entirely different behavior than their as-received counterparts. On the Mössbauer spectra of SPM NPs, the transformation of SPM doublet into a magnetic sextet is a feature of the apparition of magnetic order. Indeed, Figure 11(c) shows that the shape of the recorded spectra is in the form of a set of sextets with enough resolution to distinguish the different phases present in the sample. A better resolution was obtained with the spectrum of 77 K, and the refined model was built from it. The best fit was obtained by using three components. Obtained values of hyperfine parameters are reported in Table III, where the two components indexed as site A and site B represent the tetrahedral and octahedral site of the NFO phase, respectively, and the third component corresponds to the α-Fe$_2$O$_3$ phase. These refined hyperfine parameter values agree with those found by Kedem et al.[72] and Linnet et al.[73] Qualitatively and quantitatively, these results confirm those that we determined by XRD. Both measurements exhibit that ions Fe^{3+} are roughly evenly distributed on sites A and B, as expected for the inverse spinel ferrites. It is worth noting that there is no trace of a broad component representing the distribution of hyperfine fields for the annealed sample as was previously pointed out for lower T_A,[3,16] suggesting that in our case, the entire crystallization process had gone in the annealed NFO specimen. The second component assigned to the α-Fe$_2$O$_3$ phase is also visible at 77 K, with a slight reduction of its quantity to 48 pct compared to room temperature.

Contrary to $NiFe_2O_4$ ball-milled nanopowders, where the strongly disturbed macroscopic magnetic state was evidenced[24] in our case, the hyperfine field distribution is relatively narrow, pointing to well-crystallized spinel ferrite structure after annealing. The isomer shift (IS) values for as-received and annealed NFO samples are consistent with the high spin Fe^{3+} state.

In the case of $NFO@SiO_2$, we do not observe any trace of magnetic sextets. Here, the shape of two spectra, recorded at 300 K and 77 K, remain a quadrupolar doublet with a broad spectral line, the feature of the SPM state of ferro/ferrimagnetic nanoparticles. Before and after the annealing process, the IS values remain almost the same and are typical of a Fe^{3+} ion. Nevertheless, the observed broadening of lines and the increase of the QS value after annealing at 1000 °C show a specific structural reorganization of the $NiFe_2O_4$ phase due to the cation distribution, topological order, *etc*., favoring the appearance of a local magnetic order with a hyperfine field of the order of 2.5 T (~ 0.83 mm/s). Such a phenomenon was not observed in XRD spectra because of the dominated amount of SiO_2 shell, which covers NFO and simultaneously crystallizes itself in the annealing process, protecting NFO before crystallization. The additional surface component was already noted by Wang *et al.*,[38] who reported the existence of sextet lines up to annealing temperature of 1200 °C starting from 1000 °C, which is contrary to our studies. However, it should be noted that results presented by the authors were obtained for samples synthesized by the sol–gel method.

Similarly, Umut *et al.*[35] also evidenced an emergence of broad and rather unresolved sextet lines for $NiFe_2O_4@SiO_2$ samples explained as the influence of additional surface anisotropy induced by silica coating. Various SiO_2 thickness effects in the Fe-O-Si bonds impact the canted surface spin layer in the $NiFe_2O_4$-SiO_2 interface. For thicker SiO_2 layers, dipolar interactions between NPs are weaker than for thicker ones leading to more resolved sextet peaks due to the more substantial influence of surface anisotropy. The spin-canting effect, in this case, revealed the 28 ± 3 deg canting angle.

In addition, in our case, the hysteresis cycle, *M*(*H*) for the annealed $NFO@SiO_2$ sample indicates the significant reduction of coercivity even at low temperature at 2 K, compared to that for the as-received sample (see Figures 9(b) and (d)). Besides, the temperature evolution of the annealed $NFO@SiO_2$ specimen shows a typical SPM or paramagnetic behavior. Such a phenomenon could be interpreted as a decrease of particles sizes, but further profound studies in field Mossbauer spectrometry are needed to confirm it.

E. *Electronic Structure*

All presented XPS spectra were analyzed after Ar^+ treatment for 30 minutes with an energy beam of 1.5 keV. Before analysis, all lines were calibrated to C1s (BE = 284.8 eV) and then normalized to maximum intensity to demonstrate evident differences. Some selected lines
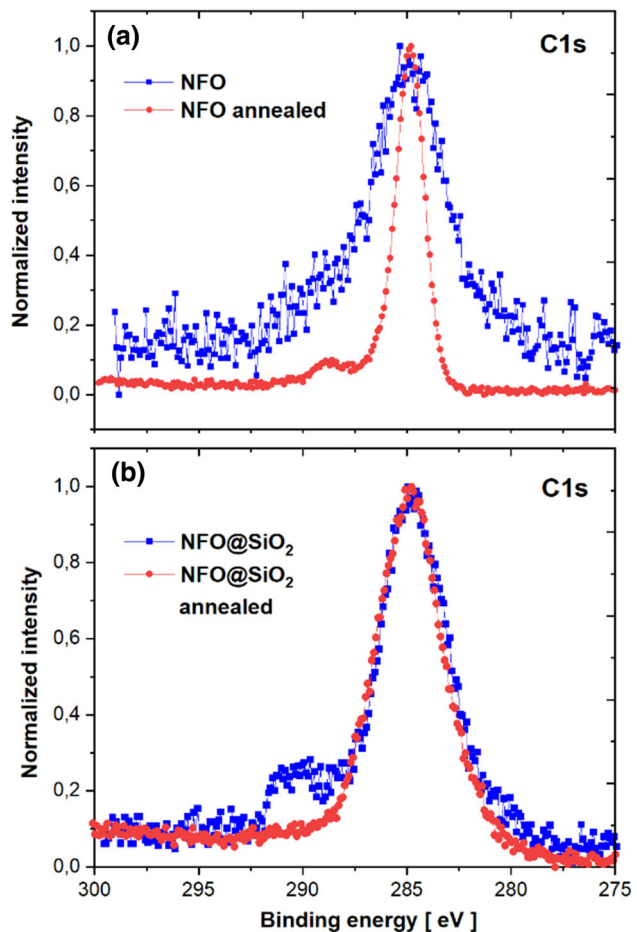

Fig. 12—Comparison between C1s states for as-received and annealed (*a*) NFO and (*b*) $NFO@SiO_2$ nanoparticles.

were further processed and fitted by the combination of the Gauss-Lorentz function and Shirley background.

The comparison between C1*s* for two compounds in their as-received and annealed form is presented in Figure 12. As one may see, the carbon line as an impurity on the surface is dominated by the sp^2 peak (C=C/C–C) at 284.8eV, which broaden at higher binding energy gives an additional contribution 286.5 eV related to the C–O–C states. Moreover, the additional shoulder visible as the low-intensity separate peak at about 288.7 eV is connected to overlapped states from carbonyl (C=O) and carboxyl (O=C–OH) groups. After annealing at ambient pressure, their contribution in each sample is different because of various crystallization processes.

The presented valence band (VB) spectra revealed the domination of O2*s* states, which are moved in both samples towards the lower binding energy range after annealing (see Figure 13). In the case of NFO, the emergence of hybridized states Ni3*d*/Fe3*d* dominated at the Fermi level (E_F) is evidently based on the valence band shape analysis. Conversely, the intensity of states on E_F for $NFO@SiO_2$ is utterly different because of the domination of O2*s* states around 26 eV from the SiO_2 matrix. The VB spectra in the vicinity of E_F visible as a
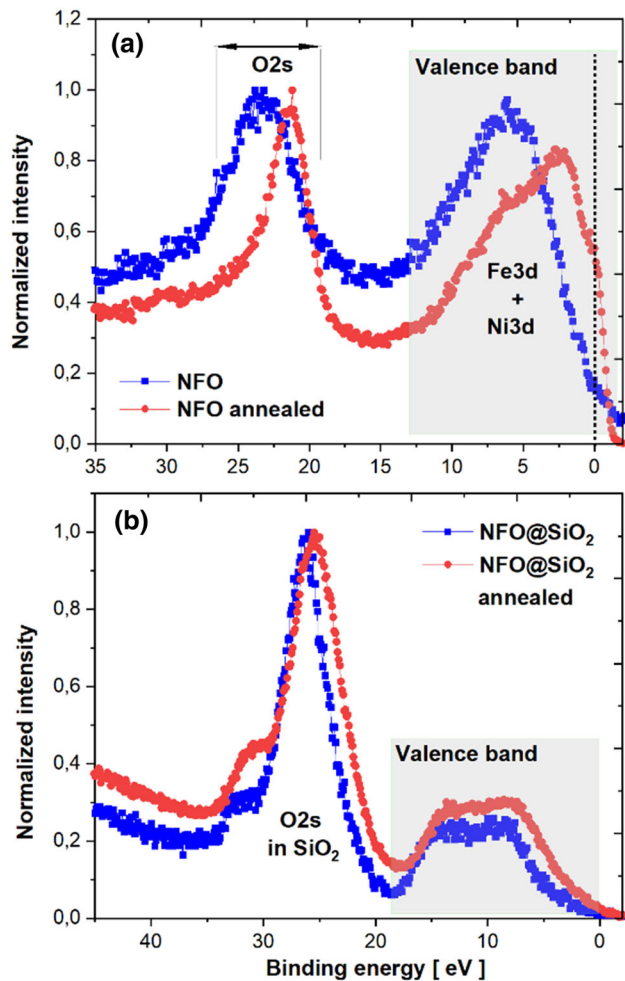
Fig. 13—Comparison between valence bands spectra for as-received and annealed (*a*) NFO and (*b*) NFO@SiO$_2$ nanoparticles.

broad band peaking around 13.2 and 8.5 eV are dominated by hybridized O2*p*, Ni3*d*/Fe3*d* states and low-intensity Si3*p*/*s* states. The presence of silica states close to E$_F$ was already demonstrated by DFT calculations made by Bagheri *et al.*[74] for SiO$_2$.

The Ni 2*p* XPS spectra for the as-received NFO sample exhibit two binding energy peaks assigned as Ni2*p$_{3/2}$* at 854.7eV and Ni2*p$_{1/2}$* at 871.8 eV with visible broad satellite peaks at around 862 and 879. eV (see Figure 14(a)). It reflects the existence of Ni^{2+} in the NiFe$_2$O$_4$ nanoparticles. The applied annealing procedure revealed the separation of pure metallic Ni peaked at around 852.5 and 869.5 eV. It is worth noting that this separation was not evidenced in XRD studies because of the different sensitivity of both techniques. In the NFO@SiO$_2$ sample, the Ni line is barely visible for the as-received sample, but the line position is similar to the NFO sample (see Figure 14(b)). The comparison of fitted Ni2*p$_{3/2}$* core level lines for both annealed specimens revealed the presence of four species (see Figures 14 (c) and (d)). For the NFO sample, the nickel spectrum is dominated by metallic Ni (BE = 852.4 eV) with a

percentage amount of about 16.2 pct. However, due to lower FWHM, the second component at BE = 854.3 eV typical for NiFe$_2$O$_4$[33,74] occupies a larger percentage area of about 31.2 pct. Two other components at BE = 857.5 eV and BE = 860.9 eV are well known for nickel-based compound 6eV satellites structure.[33,74] For the core-shell NFO@SiO$_2$ sample, the weak Ni2*p$_{3/2}$* line is also dominated by the spinel ferrite line at about 853.7 eV (40.72 pct) and almost half as much metallic nickel at 852.2 eV (23.44 pct). The 6 eV satellite structure, despite the low intensity of nickel lines, is also visible at about 855.28 and 856.36 eV, respectively.

The Fe2*p* lines presented in Figure 15 indicate the presence of Fe2*p$_{3/2}$* and Fe2*p$_{1/2}$*. In the case of as-received NFO, both lines peaked at about 712.5 and 725.1 eV are accompanied by shake-up satellites at 719.2 and 733.5 eV confirming the existence of Fe^{3+} ions in NiFe$_2$O$_4$ nanoparticles.[26,75,76] For the annealed NFO, both lines are shifted towards a lower binding energy scale because of the NFO and Fe$_2$O$_3$ phase separation, as evidenced by XRD. Thus, iron species exist in more than one chemical state. For comparison, only the Fe2*p$_{3/2}$* line for annealed samples was fitted (see Figures 15(c) and (d)), and the overall fitted curve is in good accordance with the experimental data. As one may see in the case of the NFO sample, the Fe2*p$_{3/2}$* line is composed of six quite broad and overlapped species. The one with the lowest BE is rather assigned to pure metallic Fe, whereas the other five are associated with NiFe$_2$O$_4$ and Fe$_3$O$_2$, primarily since their BE components differ practically a little, as shown by Biesinger *et al.*.[75] Generally, Fe^{3+} species in the spinel structure are related to different coordination environments, the A-tetrahedral Fe^{3+}$_{tet}$ at the higher binding energy about 711.2 eV and the B-octahedral Fe^{3+}$_{oct}$ at the lower binding energy 709.9 eV. Simultaneously both lines are accompanied by shake-up satellites around 715.3 and 713 eV, respectively.

The additional lines revealed in NFO fitting are assigned to metallic Fe (706.5 eV) and one of the Fe$_2$O$_3$ components (708.1 eV).[76,77] For the latter mentioned compound, the other lines among six detected by Biesinger *et al.*[75] are overlapped with those evidenced for NiFe$_2$O$_4$ with BE slightly different than known.[26,76,77] Thus, the ratio Fe^{3+}(A)/Fe^{3+}(B) ≈ 0.53 is significantly disturbed by the α-Fe$_2$O$_3$ contribution and the separation of Fe metallic clusters with their 6.8 pct percentage contribution. In the NFO@SiO$_2$ sample, the Fe2*p* line is weaker than in NFO by dint of the SiO$_2$ shell. Nonetheless, one may notice five components assigned to a typical inverse spinel ferrite structure with the ratio of Fe^{3+}(A)/Fe^{3+}(B) ≈ 0.8 and about 21.9 pct contribution of metallic iron. In the annealing process, the Fe line is sustained directly related to the magnetic behavior of NFO@SiO$_2$ nanoparticles.

The BE of the O1*s* orbital of the oxygen atoms in NFO below 530 eV is associated with the Ni−O and Fe−O chemical bonds in the nickel ferrite. The applied annealing causes the oxygen peak narrowing. Fitting procedures reveal four states at 529.7, 230.9, 532.3 and 533.4 eV assigned to Ni/Fe-O, C-OH, Ni/Fe-OH and
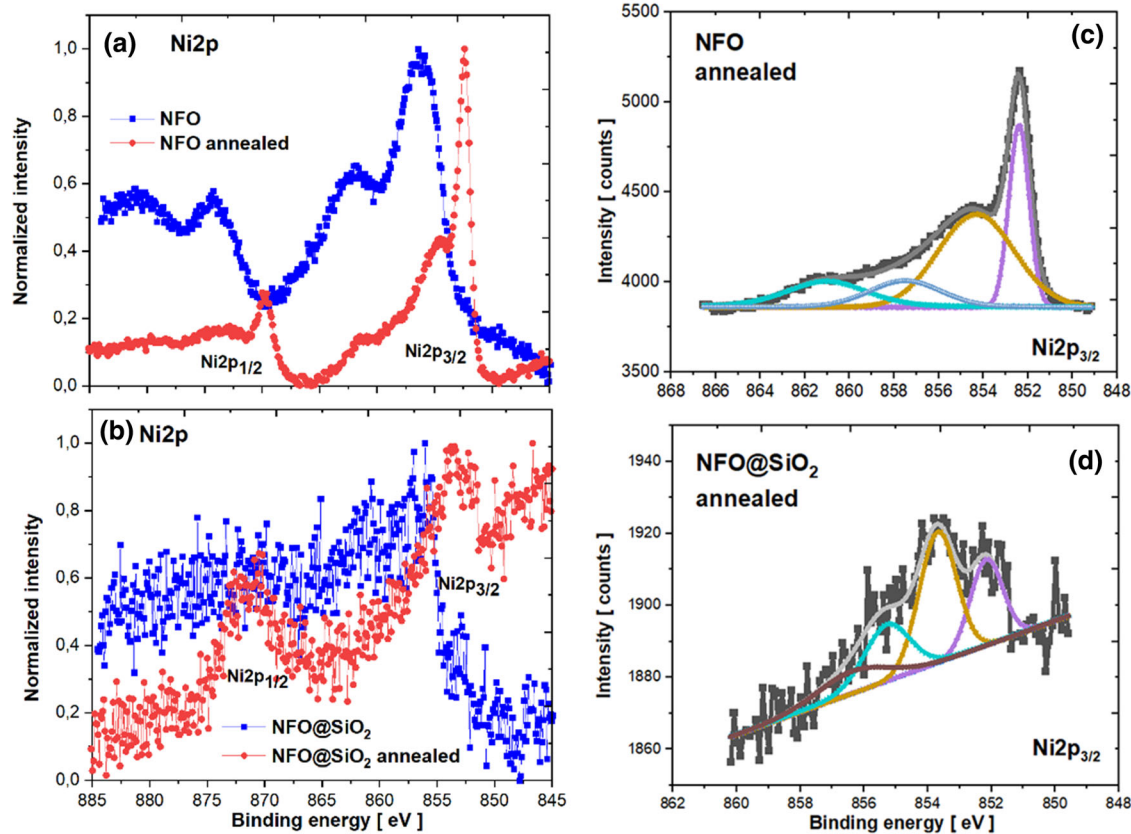
Fig. 14—Comparison between Ni2p core level lines for as-received and annealed (a) NFO and (b) NFO@SiO₂ nanoparticles. Ni2p₃/₂ core level line fit for annealed (c) NFO and (d) NFO@SiO₂ samples.

adsorbed H_2O, respectively. Among all mentioned species, the first one dominates over others occupying a percentage area of 65.3 pct. The observed structure of the O1s line is similar to that already evidenced in other ferrites.[33] As one may easily notice for the annealed NFO@SiO₂ sample, the oxygen line is shifted towards a higher BE compared to the as-received one. The evident difference is due to the domination of the silica matrix and its crystallization. Thus, the observed peaks are located at 528.1 eV (4.62 pct), 530.2 eV (21.06 pct), 532.15 eV (47.4 pct) and 533.7 eV (26.92 pct) (see Figure 16(d)). The first peak with the lowest percentage area arises from Ni/Fe-O states. The second peak from Si-O bonds is overlapped with C-OH states. So, the third dominant peak is rather related to Si-O–Si chemical bonds overlapped with Ni/Fe–OH. The last peak with the highest BE is vast as compared to the NFO sample, and its origin is not only adsorbed H_2O but mostly Si–OH chemical species. Similar O1s structures were already observed for other nanomaterials based on SiO_2.[45,78]

The analysis of the Si2p line for the NFO@SiO₂ nanocomposite reveals a slight shifting of this line into a higher binding energy range. The detailed study of such a line performed after annealing the sample shows at least four components (see Figure 17). The dominated peak placed in the middle at 103.4 eV with a percentage area of 43.44 pct is assigned to O–Si–O states over-

lapped partly with Si–O–C since the presence of the carbon line is noticeable in the sample. The line at 101.6 eV (25.75 pct) is associated with Si–O–Ni/Fe covalent bonds enhanced with the participation of Si–C. The contribution of Si–OH states as 19.36 pct is visible at 105.1 eV. The two smaller peaks at 99.6 eV (8.31 pct) and 107.6 eV (3.14 pct) are a trace of Fe3s states overlapped with pure Si and Ni3s states, respectively.

IV. CONCLUSIONS

In the present study, for the first time, we have performed the multi-technique characterization of the as-received and annealed NFO and NFO@SiO₂ nanoferrites. As shown, all physicochemical parameters in the studied samples can be tuned by the heat treatment at $T_A = 1000$ °C, enhancing the crystallization process. In all studied materials, the presence of the $NiFe_2O_4$ inverse spinel ferrite structure with A-tetrahedral and B-octahedral iron occupancy was confirmed, e.g., by infrared and photoemission spectroscopy studies. The chemical composition typical for spinel ferrites is confirmed in all measured samples by EDS spectra. For the NFO parent compound, the α-Fe_2O_3 phase was separated during annealing as evidenced by x-ray diffraction and Mössbauer spectroscopy. The gradual crystallization process of the ferrite phase is demon-
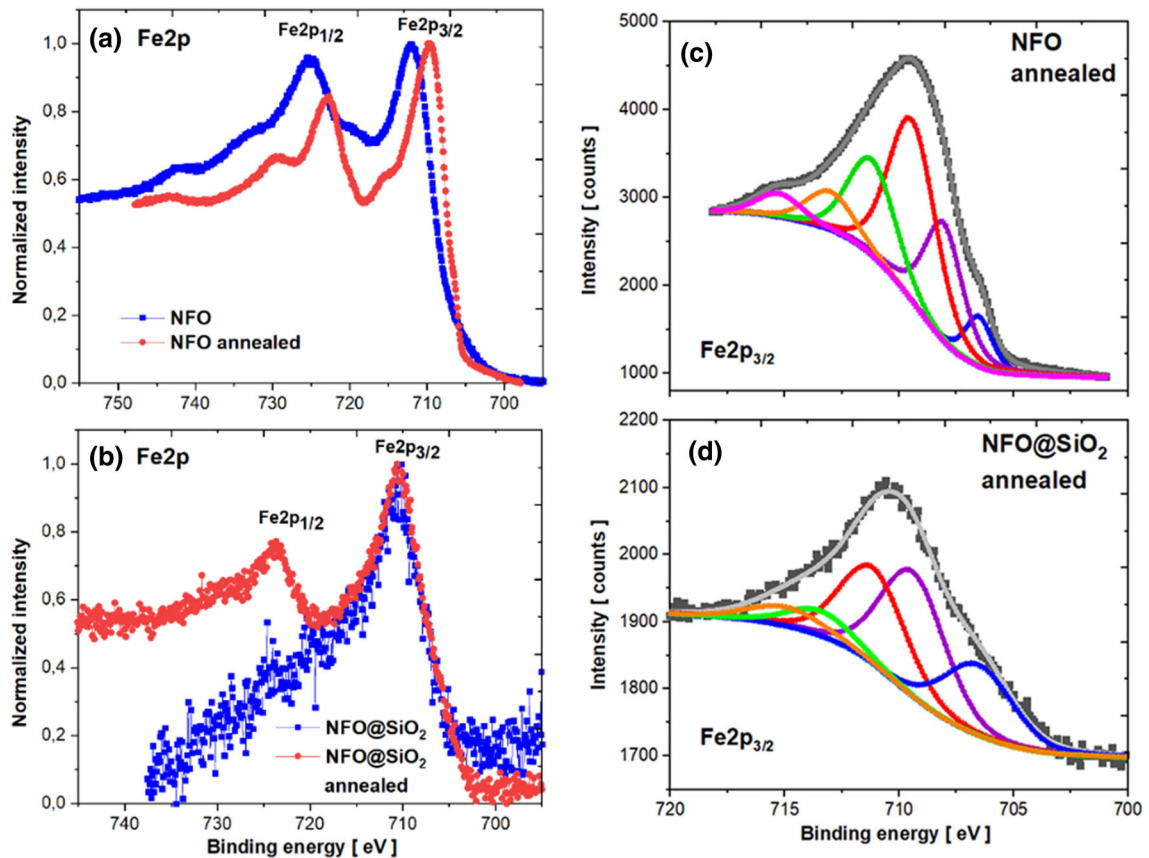
Fig. 15—Comparison between Fe2p spectra for as-received and annealed (*a*) NFO and (*b*) NFO@SiO$_2$ nanoparticles. Fe2p$_{3/2}$ core level line fit for annealed (*c*) NFO and (*d*) NFO@SiO$_2$ samples.

strated by the increase of crystallites sizes from 2.1 to 75.1 nm. For the NFO@SiO$_2$ composite, the silica matrix crystallizing itself is the protective layer for NFO. The microstructure of the NFO@SiO$_2$ sample is varied during heating from core shell (60.5 ± 0.5 nm) to thin flake particles, where the latter are in the size of hundreds of nanometers, confirming the crystallization of the silica matrix. The detailed investigation of magnetic properties exhibits the ferrimagnetic interactions between A–B sites. For the as-received NFO sample, where collective freezing is observed, the superparamagnetic behavior at room temperature is confirmed by almost zero coercivity and Mössbauer spectra. The significant changes of magnetic parameters upon annealing are associated with crystallization and hematite separation, reducing the SPM behavior due to larger than critical grain size. However, in the case of the NFO@SiO$_2$ composite, the superparamagnetic behavior is preferably supported by the silica shell, which sustains the magnetic state of ferrites. The spin canting effect was confirmed in all samples based on magnetic property measurements.

Made for the first time, the high-resolution XPS spectral analysis of core level lines in all as-received and annealed nanoferrites confirmed the distribution of Fe^{3+} at both A and B sites. Additionally, the detailed analysis of Fe2p core level lines revealed the presence of complex iron states. The modification of electronic structure is confirmed by a detailed comparison between all measured core level lines.

Therefore, first and foremost, the microstructural and magnetic properties of NiFe$_2$O$_4$ spinel nanoferrites make them natural promising and attractive candidates due to their possible applications. Furthermore, the silica shell is a protective coating for nanoferrites widening application possibilities. Undoubtedly, the applied annealing procedure favors grain growth, but parameters of this process have to be selected reasonably based on the designing of nanoparticles and their composites targeted for their potential applications.
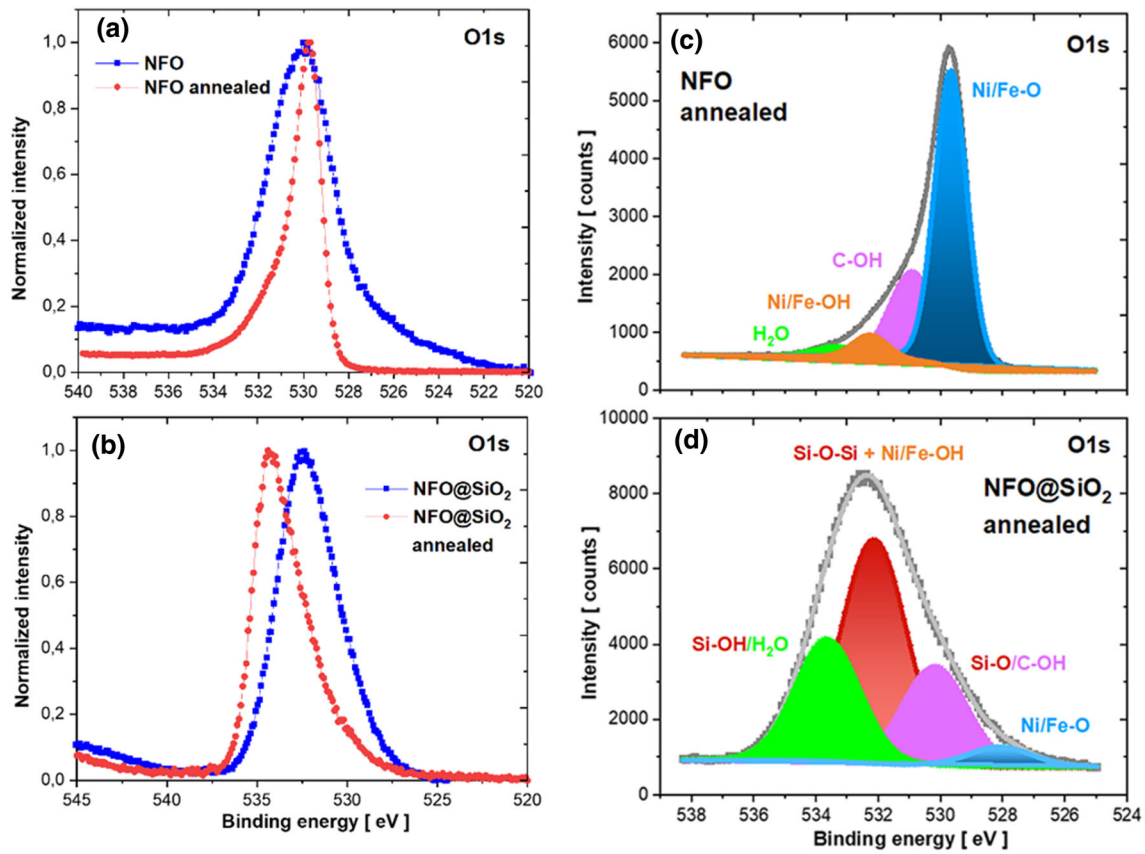
Fig. 16—Comparison of O1 spectra for as-received and annealed (*a*) NFO and (*b*) NFO@SiO$_2$ nanoparticles and chemical oxygen states for annealed (*c*) NFO and (*d*) NFO@SiO$_2$ samples.
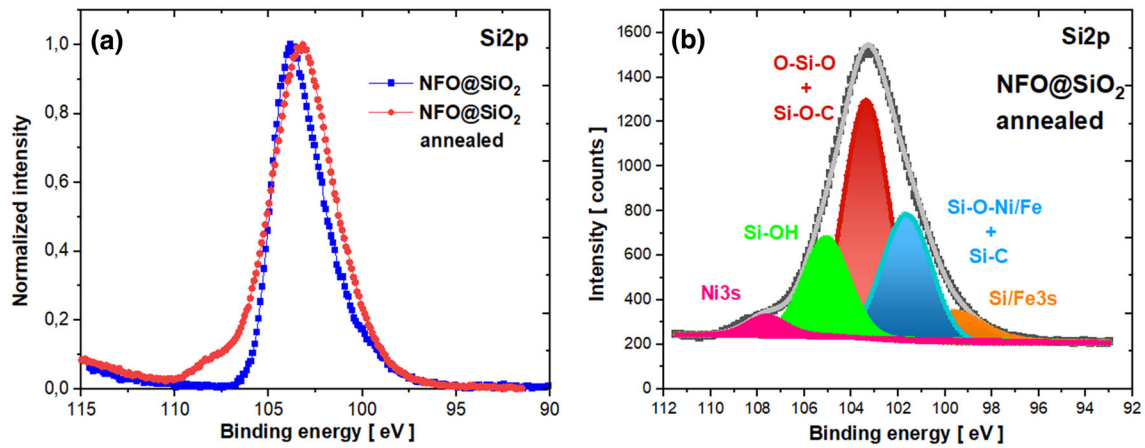

Fig. 17—(*a*) Comparison of Si2p spectra for as-received and annealed NFO@SiO$_2$ nanoparticles. (*b*) Silicon chemical states for annealed NFO@SiO$_2$ sample.

CONFLICT OF INTEREST

The authors declare that they have no known competing financial interests or personal relationships that could have appeared to influence the work reported in this paper

OPEN ACCESS

REFERENCES

1. M.S. Seehra ed.: *Magnetic Spinels—Synthesis, Properties and Applications*, InTechOpen, Rijeka, Croatia, 2017.
2. M. Tsvetkov, M. Milanova, L.C.J. Pereira, J.C. Waerenbourgh, Z. Cherkezova-Zheleva, J. Zaharieva, and I. Mitov: *Chem. Pap.*, 2016, vol. 70, pp. 1600–10.
3. Y.G.G. Ma, M.Z. Jin, M.L. Liu, G. Chen, Y. Sui, Y. Tian, G.J. Zhang, and Y.Q. Jia: *Mater. Chem. Phys.*, 2000, vol. 65, pp. 79–84.
4. J. Huo and M. Wei: *Mater. Lett.*, 2009, vol. 63, pp. 1183–84.
5. J. Wang, F. Ren, R. Yi, A. Yan, G. Qiu, and X. Liu: *J. Alloys Compd.*, 2009, vol. 479, pp. 791–96.
6. K. Maaz, S. Karim, A. Mumtaz, S.K. Hasanain, J. Liu, and J.L. Duan: *J. Magn. Magn. Mater.*, 2009, vol. 321, pp. 1838–42.
7. P. Sivakumar, R. Ramesh, A. Ramanand, S. Ponnusamy, and C. Muthamizhchelvan: *Mater. Res. Bull.*, 2011, vol. 46, pp. 2204–07.
8. C. Luadthong, V. Itthibenchapong, N. Viriya-Empikul, K. Faungnawakij, P. Pavasant, and W. Tanthapanichakoon: *Mater. Chem. Phys.*, 2013, vol. 143, pp. 203–08.
9. M.I. Oshtrakh, M.V. Ushakov, B. Senthilkumar, R.K. Selvan, C. Sanjeeviraja, I. Felner, and V.A. Semionkin: *Hyperfine Interact.*, 2013, vol. 219, pp. 7–12.
10. M. Kooti and A.N. Sedeh: *J. Mater. Sci. Technol.*, 2013, vol. 29, pp. 34–38.
11. D. Li, Y. Sun, P. Gao, X. Zhang, and H. Ge: *Ceram. Int.*, 2014, vol. 40, pp. 16529–34.
12. T. Shanmugavel, S.G. Raj, G. Rajarajan, and G.R. Kumar: *Procedia Mater. Sci.*, 2014, vol. 6, pp. 1725–30.
13. Z. Cvejić, E. Đurđić, G. Ivković Ivandekić, B. Bajac, P. Postolache, and L. Mitoseriu: *J. Alloys. Compd.*, 2015, vol. 649, pp. 1231–38.
14. T. Shanmugavel, S. Gokul Raj, G. Ramesh Kumar, G. Rajarajan, and D. Saravanan: *J. King Saud Univ. Sci.*, 2015, vol. 27, pp. 176–81.
15. N. Gupta, P. Jain, R. Rana, and S. Shrivastava: *Mater. Today Proc.*, 2017, vol. 4, pp. 342–49.
16. S.M. Hoque, M. Tariq, S.I. Liba, F. Salehin, Z.H. Mahmood, M.N.I. Khan, K. Chattopadhayay, R. Islam, and S. Akhter: *Nanotechnology*, 2016, vol. 27, p. 285702.
17. E. Agouriane, A. Essoumhi, A. Razouk, M. Sahlaoui, and M. Sajieddine: *J. Mater. Environ. Sci.*, 2016, vol. 7, pp. 4614–19.
18. A. Sangeetha, K. Vijaya Kumar, and G. Nanda Kumar: *Adv. Mater. Phys. Chem.*, 2017, vol. 7, pp. 19–27.
19. Z.Ž. Lazarević, Č. Jovalekić, A. Milutinović, D. Sekulić, V.N. Ivanovski, A. Rečnik, B. Cekić, and N.Ž. Romčević: *J. Appl. Phys.*, 2013, vol. 113, p. 187221.
20. R. Kurosawa, T. Suzuki, T. Nakayama, H. Suematsu, K. Niihara, Y.K. Jeong, and K.H. Kim: *Curr. Appl. Phys.*, 2012, vol. 12, pp. S68–S70.
21. N. Shara Sowmya, A. Srinivas, P. Saravanan, K. Venu Gopal Reddy, M. Vinitha Reddy, D. Das, and S.V. Kamat: *J. Magn. Magn. Mater.*, 2017, vol. 436, pp. 31–34.
22. K.V.P.M. Shafi, Y. Koltypin, A. Gedanken, R. Prozorov, J. Balogh, J. Lendvai, and I. Felner: *J. Phys. Chem. B*, 1997, vol. 101, pp. 6409–14.
23. G. Nabiyouni, M. Jafari Fesharaki, M. Mozafari, and J. Amighian: *Chin. Phys. Lett.*, 2010, vol. 27, p. 126401.
24. V. Šepelák, I. Bergmann, A. Feldhoff, P. Heitjans, F. Krumeich, D. Menzel, F.J. Litterst, S.J. Campbell, and K.D. Becker: *J. Phys. Chem. C*, 2007, vol. 111, pp. 5026–33.
25. J.Z. Msomi, T. Moyo, and J.J. Dolo: *Hyperfine Interact.*, 2010, vol. 197, pp. 59–64.
26. A. Bajorek, C. Berger, M. Dulski, P. opadczak, M. Zubko, K. Prusik, M. Wojtyniak, A. Chrobak, F. Grasset, and N. Randrianantoandro: *J. Phys. Chem. Solids*, 2019, vol. 129, pp. 1–21.
27. H. Kavas, A. Baykal, M.S. Toprak, Y. Köseoğlu, M. Sertkol, and B. Aktaş: *J. Alloys Compd.*, 2009, vol. 479, pp. 49–55.
28. T. Slatineanu, A.R. Iordan, M.N. Palamaru, O.F. Caltun, V. Gafton, and L. Leontie: *Mater. Res. Bull.*, 2011, vol. 46, pp. 1455–60.
29. A. Ahlawat, V.G. Sathe, V.R. Reddy, and A. Gupta: *J. Magn. Magn. Mater.*, 2011, vol. 323, pp. 2049–54.
30. C.N. Chinnasamy, A. Narayanasamy, N. Ponpandian, K. Chattopadhyay, K. Shinoda, B. Jeyadevan, K. Tohji, K. Nakatsuka, T. Furubayashi, and I. Nakatani: *Phys. Rev. B*, 2001, vol. 63, p. 184108.
31. R.S. Yadav, I. Kuřitka, J. Vilcakova, J. Havlica, J. Masilko, L. Kalina, J. Tkacz, V. Enev, and M. Hajdúchová: *J. Phys. Chem. Solids*, 2017, vol. 107, pp. 150–61.
32. O.V. Yelenich, S.O. Solopan, T.V. Kolodiazhnyi, V.V. Dzyublyuk, A.I. Tovstolytkin, and A.G. Belous: *Solid State Sci.*, 2013, vol. 20, pp. 115–19.
33. J.-L. Ortiz-Quiñonez, U. Pal, and M. Salazar Villanueva: *ACS Omega*, 2018, vol. 3, pp. 14986–15001.
34. A.S. Kamzin, A. Bingolbali, N. Doğan, Z. Yeşil, and M. Asiltürk: *Tech. Phys. Lett.*, 2019, vol. 45, pp. 1008–11.
35. E. Umut, M. Coşkun, H. Güngüneş, V. Dupuis, and A.S. Kamzin: *J. Supercond. Nov. Magn.*, 2021, vol. 34, pp. 913–24.
36. A. Chaudhuri, M. Mandal, and K. Mandal: *J. Alloys Compd.*, 2009, vol. 487, pp. 698–702.
37. N. Shukla, A. Ondeck, J.C. Lee, and J.B. Mille: *Catal. Lett.*, 2021, vol. 142, pp. 582–87.
38. L. Wang, J. Li, M. Lu, H. Dong, J. Hua, S. Xu, and H. Li: *J. Supercond. Nov. Magn.*, 2015, vol. 28, pp. 191–96.
39. S. Mitra, K. Mandal, and P. Anil Kumar: *J. Magn. Magn. Mater.*, 2006, vol. 306, pp. 254–59.
40. S. Balamurugan, M. Durga Devi, I. Prakash, and S. Devaraj: *Appl. Surf. Sci.*, 2018, vol. 449, pp. 542–50.
41. M. Gharagozlou: *J. Alloys Compd.*, 2010, vol. 495, pp. 217–23.
42. G. Pozo López, S.P. Silvetti, S.E. Urreta, and A.C. Carreras: *J. Alloys Compd.*, 2010, vol. 505, pp. 808–13.
43. G. Pozo López, S.P. Silvetti, M. del C. Aguirre and A.M. Condó: *J. Alloys Compd.*, vol. 487, pp. 646–652.
44. L. Li, G. Li, R.L. Smith, and H. Inomata: *Chem. Mater.*, 2000, vol. 12, pp. 3705–14.
45. H. Fu, X. Ding, C. Ren, W. Li, H. Wu, and H. Yang: *RSC Adv.*, 2017, vol. 7, pp. 16513–23.
46. J.-P. Jolivet, M. Henry, J. Livage: *De la solution à l'oxyde: condensation des cations en solution aqueuse, chimie de surface des oxydes*, InterÉditions CNRS: éditions EDP Sciences, Paris, 1994.

47. F. Grasset, N. Labhsetwar, D. Li, D.C. Park, N. Saito, H. Haneda, O. Cador, T. Roisnel, S. Mornet, E. Duguet, J. Portier, and J. Etourneau: *Langmuir*, 2002, vol. 18, pp. 8209–16.
48. T. Aubert, F. Grasset, S. Mornet, E. Duguet, O. Cador, S. Cordier, Y. Molard, V. Demange, M. Mortier, and H. Haneda: *J. Colloid Interface Sci.*, 2020, vol. 341, pp. 201–08.
49. S.E. Shirsath, B.G. Toksha, R.H. Kadam, S.M. Patange, D.R. Mane, G.S. Jangam, and A Ghasemi: *J. Phys. Chem. Solids*, 2010, vol. 71, pp. 1669–75.
50. H. Fan, B. Song, Z. Yang, and Q. Li: *Nanotechnology*, 2005, vol. 16, pp. 1100–04.
51. A.A. Khaleel: *Chemistry*, 2004, vol. 10, pp. 925–32.
52. S.J. Oh, D.C. Cook, and H.E. Townsend: *Hyperfine Interact.*, 1998, vol. 112, pp. 59–66.
53. U. Schwertmann and W.R. Fischer: *Geoderma*, 1973, vol. 10, pp. 237–47.
54. A. Voegelin and S.J. Hug: *Environ. Sci. Technol.*, 2003, vol. 37, pp. 972–78.
55. D. Walter, G. Buxbaum, and W. Laqua: *J. Therm. Anal. Calorim.*, 2001, vol. 63, pp. 733–48.
56. H. Fan, B. Song, and Q. Li: *Mater. Chem. Phys.*, 2006, vol. 98, pp. 148–53.
57. P.S.R. Prasad, K. Shiva Prasad, V. Krishna Chaitanya, E.V.S.S.K. Babu, B. Sreedhar, and S. Ramana Murthy: *J. Asian Earth Sci.*, 2006, vol. 27, pp. 503–11.
58. I.V. Chernyshova, M.F. Hochella, Jr, and A.S. Madden: *Phys. Chem. Chem. Phys.*, 2007, vol. 9, pp. 1736–50.
59. A. Ebrahiminezhad, Y. Ghasemi, S. Rasoul-Amini, J. Barar, and S. Davaran: *Bull. Korean Chem. Soc.*, 2012, vol. 33, pp. 3957–63.
60. S. Ramalingam, L.B. Devi, J. Rao, and B.U. Nair: *RSC Adv.*, 2014, vol. 4, pp. 56041–51.
61. F. Zhao, X. Wang, B. Ding, J. Lin, J. Hu, Y. Si, J. Yu, and G. Sun: *RSC Adv.*, 2011, vol. 1, pp. 1482–88.
62. H. Moghanian, A. Mobinikhaledi, A.G. Blackmanc, and E. Sarough-Farahani: *RSC Adv.*, 2014, vol. 4, pp. 28176–85.
63. Y. Liang, C. Miranda, and S. Scandolo: *J. Chem. Phys.*, 2006, vol. 125, p. 19452.
64. G.C. Koike, R. Noguchi, H. Chihara, H. Suto, O. Ohataka, Y. Imai, T. Matsumoto, and A. Tsuchiyama: *Astrophys. J.*, 2013, vol. 778, p. 1.
65. B. Aslibeiki, P. Kameli, and H. Salamati: *J. Appl. Phys.*, 2016, vol. 119, p. 063901.
66. M. Knobel, W.C. Nunes, L.M. Socolovsky, E. De Biasi, J.M. Vargas, and J.C. Denardin: *J. Nanosci. Nanotechnol.*, 2008, vol. 8, pp. 2836–57.
67. M. Tadić, N. Čitaković, M. Panjan, Z. Stojanović, D. Marković, and V. Spasojevic: *J. Alloys Compd.*, 2001, vol. 509, pp. 7639–44.
68. P. Fabrykiewicz, M. Stekiel, I. Sosnowska, and R. Przenioso: *Acta Cryst.*, 2017, vol. B73, pp. 27–32.
69. R. Topkaya, A. Baykal, and A. Demir: *J. Nanoparticle Res.*, 2013, vol. 15, p. 1359.
70. Y. Yafet and C. Kittel: *Phys. Rev. B*, 1952, vol. 87, pp. 290–94.
71. R.H. Kodama and A.E. Berkowitz: *Phys. Rev. B*, 1999, vol. 59, pp. 6321–36.
72. D. Kedem and T. Rothem: *Phys. Rev. Lett.*, 1967, vol. 18, pp. 165–66.
73. J.W. Linnett and M.M. Rahman: *J. Phys. Chem. Solids*, 1972, vol. 33, pp. 1465–73.
74. M. Bagheri and P. Blaha: *J. Electron Spectrosc. Relat. Phenom.*, 2019, vol. 230, pp. 1–9.
75. M.C. Biesinger, B.P. Payne, A.P. Grosvenor, L.W.M. Lau, A.R. Gerson, and R.S.T.C. Smart: *Appl. Surf. Sci.*, 2011, vol. 257, pp. 2717–30.
76. A.P. Grosvenor, B.A. Kobe, M.C. Biesinger, and N.S. McIntyre: *Surf. Interface Anal.*, 2004, vol. 36, pp. 1564–74.
77. A. Bajorek, B. Liszka, B. Szostak, and M. Pawlyta: *J. Magn. Magn. Mater.*, 2020, vol. 503, p. 166634.
78. A. Hashemi and A. Bahari: *Appl. Phys. A*, 2017, vol. 123, p. 535.